Nulling Control Beamforming for MU-mMIMO

Arish Yaseen

Department of Electrical & Computer Engineering
McGill University
Montréal, Québec, Canada

February 2025

A thesis submitted to McGill University in partial fulfillment of the requirements of the degree of Master of Science

To my parents,
With all my love.

Abstract

The exponential growth of wireless devices has led to increased demand for high-speed data transmission, exacerbating bandwidth shortages and creating challenges in managing connections between base stations and densely deployed users. Massive multiple-input multiple-output (mMIMO) technology addresses these challenges by utilizing large-scale phased antenna arrays to serve multiple users simultaneously. However, unintended radiation in non-target directions leads to Multi-User Interference (MUI) and degrades overall system performance. Current Nulling Control Beamforming (NCB) methods, such as Linear Constraint Minimum Variance (LCMV), attempt to mitigate interference by steering nulls toward interfering users to improve the Signal-to-Interference-plus-Noise Ratio (SINR). However, these methods assume uniform element radiation patterns (ERPs), an assumption rarely met in real-world systems, resulting in reduced accuracy and effectiveness.

This thesis explores array processing theory to analyze the factors affecting beam radiation patterns. It investigates the performance of LCMV beamforming with non-uniform antenna ERPs using measured ERP data from an 8x8 antenna array in simulations. The results clearly link increased ERP variation and reduced LCMV performance, particularly in achieving deep and precise nulls toward interference sources. Furthermore, LCMV struggles to maintain beam shape and high SINR in the presence of multiple interfering users, highlighting its limitations in practical deployments.

To overcome these limitations, this thesis presents a Perturbation-based Nulling Control Beamforming (PNCB) method, which integrates the LCMV framework with Particle Swarm Optimization (PSO) to iteratively refine beamforming weights. The PNCB approach takes into account non-uniform ERPs and incorporates quantization to address practical hardware limitations. Starting with LCMV-generated weights, PSO performs a

global optimization within defined magnitude and phase boundaries to achieve optimal beamforming. Simulation results illustrate that the proposed PNCB method achieves significantly deeper nulls compared to LCMV in multi-user scenarios while maintaining a consistent power level toward the target user. Additionally, experimental validation using a 20 MHz modulated signal in an anechoic chamber confirmed the practical advantages of PNCB. Overall, PNCB consistently delivers superior SINR, even in challenging scenarios involving non-uniform ERPs and multiple interfering users.

Abrégé

La croissance exponentielle des appareils sans fil a conduit à une demande accrue de transmission de données à haut débit, exacerbant les pénuries de bande passante et créant des défis dans la gestion des connexions entre les stations de base et les utilisateurs déployés de manière dense. La technologie massive à entrées multiples et sorties multiples (mMIMO) répond à ces défis en utilisant des réseaux d'antennes phasées à grande échelle pour servir simultanément plusieurs utilisateurs. Cependant, le rayonnement non intentionnel dans des directions non ciblées entraîne des interférences multi-utilisateurs (MUI) et dégrade les performances globales du système. Les méthodes actuelles de contrôle de formation de faisceaux avec annulation (NCB), telles que la méthode de variance minimale à contrainte linéaire (LCMV), tentent de réduire les interférences en orientant des nuls vers les utilisateurs interférents afin d'améliorer le rapport signal sur interférence plus bruit (SINR). Cependant, ces méthodes supposent des schémas de rayonnement uniformes des éléments d'antenne (ERP), une hypothèse rarement vérifiée dans les systèmes réels, ce qui entraîne une réduction de la précision et de l'efficacité.

Cette thèse explore la théorie du traitement de réseau pour analyser les facteurs affectant les schémas de rayonnement de faisceau. Elle étudie les performances de la formation de faisceaux LCMV avec des ERPs d'antennes non uniformes en utilisant des données mesurées d'un réseau d'antennes 8x8 dans des simulations. Les résultats montrent clairement un lien entre l'augmentation de la variation des ERPs et la diminution des performances du LCMV, notamment dans la capacité à atteindre des nuls profonds et précis en direction des sources d'interférence. De plus, LCMV éprouve des difficultés à maintenir la forme du faisceau et un SINR élevé en présence de plusieurs utilisateurs interférents, soulignant ses limites dans les déploiements pratiques.

Pour surmonter ces limitations, cette thèse présente une méthode de formation de

faisceaux de contrôle d'annulation basée sur la perturbation (PNCB), qui intègre le cadre LCMV avec l'optimisation par essaims particulaires (PSO) pour affiner itérativement les poids de formation de faisceaux. L'approche PNCB prend en compte les ERPs non uniformes et intègre la quantification pour répondre aux contraintes matérielles pratiques. En partant des poids générés par LCMV, PSO effectue une optimisation globale dans des limites de magnitude et de phase définies pour atteindre la formation de faisceaux optimale. Les résultats de simulation illustrent que la méthode PNCB proposée atteint des nuls significativement plus profonds par rapport au LCMV dans des scénarios multi-utilisateurs tout en maintenant un niveau de puissance constant vers l'utilisateur cible. En outre, une validation expérimentale utilisant un signal modulé de 20 MHz dans une chambre anéchoïque a confirmé les avantages pratiques de PNCB. Dans l'ensemble, PNCB fournit constamment un SINR supérieur, même dans des scénarios complexes impliquant des ERPs non uniformes et de multiples utilisateurs interférents.

Acknowledgment

I would like to express my deepest gratitude and appreciation to my supervisor, Dr. Tho Le-Ngoc. His support and guidance have been instrumental in the completion of this thesis. Dr. Le-Ngoc has been an inspirational and motivational figure, and I have learned immensely from his research expertise, creativity, work ethic, and dedication. Without his unwavering support and enthusiasm, this work would not have been possible.

I would like to extend my sincere thanks to the McGill Graduate Excellence Fellowship (GEF), the Natural Sciences and Engineering Research Council (NSERC) of Canada, and Huawei Technologies for their financial support throughout my research journey.

I also wish to acknowledge the valuable collaboration with my colleague, Yuanzhe Gong. I am immensely grateful for his constructive advice, patience, and helpful comments during my whole research and writing. My thanks also go to our lab in-charge, Robert Mowraski, for his continuous guidance on hardware components and measurements. Additionally, I am profoundly thankful to my friends, Farzan, Mobeen, and Farhan, at the Broadband Communications Research Lab (BCRL), for their camaraderie and support.

Furthermore, I want to thank my friends Gunel, Saad and Hamza for their unwavering encouragement and for cheering me on during challenging times.

Lastly, and most importantly, I am deeply grateful to my parents, my sister, and my entire family (Yaseen, Afshan, Aqsa) for their unconditional love and support throughout my life. This thesis is dedicated to my parents, whose encouragement and sacrifices have been the foundation of my achievements. Their belief in me has been my greatest source of strength in pursuing my dreams, and I owe this accomplishment to them.

Contribution of Author

In all chapters of this thesis, except Sections 3.2.1, 4.1, and 4.3, the author formulated the problem, developed the simulations, performed the analysis of the results, and wrote the manuscript.

For the content in Section 3.2.1, Yuanzhe Gong designed the antenna board and proposed the measurement method. The author assisted in conducting the measurements, recorded the results, and contributed to improving the manuscript. For Section 4.1, Yuanzhe Gong assisted in problem formulation and defining the problem flow. For Section 4.3, Yuanzhe Gong and Robert Mowraski assisted in setting up the experiment and measuring the results.

Parts of the contributions from Chapter 4 have been published as follows:

- [1] Y. Gong, A. Yaseen, R. Morawski and T. Le-Ngoc, "Perturbation-Based Adaptive Beamforming for MU-mMIMO," 2023 IEEE 98th Vehicular Technology Conference (VTC2023-Fall), Hong Kong, Hong Kong, 2023, pp. 1-5.
- [2] Y. Gong, A. Yaseen, T. Zhang, R. Morawski and T. Le-Ngoc, "Perturbation-Based Nulling Control Beamforming With Measured Element Radiation Patterns for MU-mMIMO," in IEEE Open Journal of Vehicular Technology, vol. 5, pp. 1273-1293, 2024.

In both mentioned publications, the author contributed by assisting in problem formulation, running the simulations, assisting in measurements, verifying and analyzing the results, and revising the manuscript. In both papers, Prof. Tho Le-Ngoc proposed the research subjects, supervised the works, and assisted with editing and writing the manuscripts.

Contents

List of Figures

List of Tables

List of Acronyms

ABF	Adaptive beamforming.
ADC	Analogue to digital converters.
AF	Array factor.
AR-BF	Analogue radio-frequence beamforming.
AWGN	Additive white guassian noise.
BA	Bees Algorithm.
BF	Beamforming.
BFA	Bacteria-Foraging Algorithm.
BFNC	Beamforming Network Controller.
BS	Base station.
CLPSO	Comprehensive Learning Particle Swarm Optimization.
CMA	Constant modulus algorithm.
CP	Circularly polarized.
CS	Compressed sensing.
DAC	Digital-to-Analogue Converter.
DB-BF	Digital baseband beamformer.
DM-AIS	Dynamic Mutated Artificial Immune System.
DoA	Direction of arrival.
EBG	Electromagnetic bandgap.
ERP	Element radiation pattern.
EVD	Eigen value decomposition.
FDB	Fully digital beamforming.
FFT	Fast Fourier Transform.
FNBW	First null beamwidth.

GA	Genetic Algorithm.
GSA	Gravitational Search Algorithm.
HBF	Hybrid beamforming.
LCMV	Linear Constraint Minimum Variance.
LLMS	Least mean square - least mean square.
LMS	Least Mean Square.
MDBF	Maximum directivity beamforming.
mMIMO	Massive multiple input multiple output.
MSE	Mean square error.
MU	Multi-user.
MUI	Multi-user interference.
MU-mMIMO	Multi user massive multiple input multiple output.
MVDR	Minimum variance distortionless response.
NCB	Nulling control beamforming.
PNCB	Perturbation-based Nulling Control Beamforming.
PSO	Particle Swarm Optimization.
RF	Radio frequency.
RLS	Recursive least square.
RPI-4B	Raspberry Pi 4B.
Rx	Receiver.
SINR	Signal-to-interference-plus-noise ratio.
SNR	Signal-to-noise ratio.
SPC	Serial-to-Parallel Converter.
SPI	Serial Peripheral Interface.
Tx	Transmitter.
ULA	Uniform linear array.
URLLC	Ultra-reliable low-latency communication.
VNA	Vector network analyzer.

List of Symbols

N_{rf}	Number of RF chains
N_s	Number of data streams
M	Number of antenna elements
d	Distance between two consecutive antenna elements
D	User location in Far Field
D_r	Rayleigh distance
λ_0	Wavelength of signal
θ	Azimuth angle
ϕ	Elevation angle
f_c	Carrier frequency
ω_c	Carrier angular frequency
c	Speed of light
ζ	Inter-element phase shift
β	Phase constant
t	Time
s'	Incoming modulated signal

a	Incoming modulated signal amplitude
Φ	Incoming modulated signal Phase shift
s	Equivalent complex baseband signal of s'
r'	Received modulated signal
r	Equivalent complex baseband signal of r'
E	Normalized ERP
n'	Received Guassian thermal noise signal
n	Equivalent complex baseband signal of n'
σ_n^2	Gussian noise power
$\mathbf{w}$	Beamforming Vector, $\in \mathbb{C}^{M\times 1}$
W_m	Magnitude of beamforming weight w_m
ψ	Phase shift added by beamforming weight
$\boldsymbol{a}$	Steering Vector, $\in \mathbb{C}^{M\times 1}$
$\boldsymbol{n}$	Noise Vector, $\in \mathbb{C}^{M\times 1}$
A	Array Factor
Ψ	Phase shift caused by array factor
$\mathbf{R}$	Noise Covariance Matrix, $\in \mathbb{C}^{M\times M}$
P_n	Power of output noise
K_c	Number of directions with linear constraints
$\mathbf{C}$	Constraint Matrix, $\in \mathbb{C}^{M\times K_c}$
$\boldsymbol{g}$	Constraint Gain Vector, $\in \mathbb{C}^{K_c\times 1}$

$\mathbf{I}$	Identity Matrix
λ	Lagrange Multiplier
K	Number of User Entities
θ_i	Target user direction
θ_N	Interference user direction
$\boldsymbol{\theta}_N$	Vector of Potential interference directions
$\boldsymbol{t}_i$	Transmitted Signal from i^{th} subarray
$\mathcal{A}(\boldsymbol{\theta}_N)$	Interference steering matrix $\mathbb{C}^{M\times(K-1)}$
g	High power gain
$\mathbf{E}_m$	Normalized ERP matrix for m^{th} element, $\in \mathbb{R}^{361\times181}$
Ω	PSO search vector, $\in \mathbb{R}^{2M}$
Ω_{LCMV}	Search vector derived from LCMV-generated weights
N_p	Number of particles
N_n	Maximum number of iterations
N_s	Maximum number of stall iterations
Q	Penalty Factor
ϵ	Directivity trade off tolerance
$\boldsymbol{\gamma}$	Random real valued vector, $\in \mathbb{R}^{1\times(K-1)}$
χ	Random real valued scalar
Δv	Maximum allowable phase shift
δ	Velocity vector of particles, $\in \mathbb{R}^{2M}$

$\mathbf{J}$	Diagonal weight matrix to define particles' inertia, $\in \mathbb{R}^{2M \times 2M}$
$\mathbf{K}$	Diagonal random-valued matrix to define particles' self-adjustment, $\in \mathbb{R}^{2M \times 2M}$
$\mathbf{L}$	Diagonal random-valued matrix to define particles' social-adjustment, $\in \mathbb{R}^{2M \times 2M}$
Ω_L	PSO search vector lower bounds
Ω_U	PSO search vector upper bounds
Q_p	Phase shifter resolution bits
Q_t	Attenuator resolution bits
D(.)	Function to provide directivity at given beamforming weight and angle(s)
mag(.)	Function to get magnitude of the given beamforming vector
ang(.)	Function to get phase of the given beamforming vector
clip(.)	Function to clip the value within the given bounds

Chapter 1

Introduction

The use of a large number of antenna elements in mMIMO systems significantly enhances the spatial degrees of freedom, enabling the formation of highly directional and narrow beams. These narrow beams help minimize interference between users and improve signal focus, allowing mMIMO to efficiently serve multiple target users in a dense user environment. Additionally, large-scale mMIMO systems can operate as multi-user mMIMO (MU-mMIMO), where the array is divided into multiple subarrays that simultaneously transmit and receive distinct data streams over the same frequency band in a full-duplex manner. This capability greatly enhances spectral efficiency and increases the system's multi-user capacity, making mMIMO suitable for modern wireless networks requiring high throughput and user density [3, 4].

In MU-mMIMO systems, the fully digital beamformer (FDB) offers the advantage of providing maximum flexibility by requiring one distinct radio frequency (RF) chain per antenna element. This setup allows precise control over the phase and amplitude of each antenna, enabling optimal beamforming, improved interference mitigation, and support for advanced signal processing techniques like multi-user beamforming. However, the main disadvantage of FDB in large-scale mMIMO systems is the significant power consumption and high operational costs due to the need for a large number of RF chains, analog-to-digital converters (ADCs) and other hardware components to match a large number of antennas [5]. Real-world implementations of FDB often face issues with thermal management due to the increased heat dissipation in systems with many RF chains. Additionally, the complexity of synchronizing a large number of chains without introducing latency becomes a significant

challenge, especially in environments requiring ultra-reliable low-latency communications (URLLC). This makes FDB less practical for large-scale antenna arrays, especially in cost-sensitive or power-limited applications.

Since the number of required beams is equal to the much smaller number of multiple users to be served simultaneously, the required number of RF chains can be reduced, which suggests the Hybrid Beamforming (HBF) architectures. HBF architectures combine analog RF beamforming (AR-BF) with digital baseband beamforming (DB-BF), in which the number of RF chains (N_{RF}) is determined by the number of data streams (N_s) rather than the number of antennas (M), making this approach more cost-effective for large-scale mMIMO [6, 7].

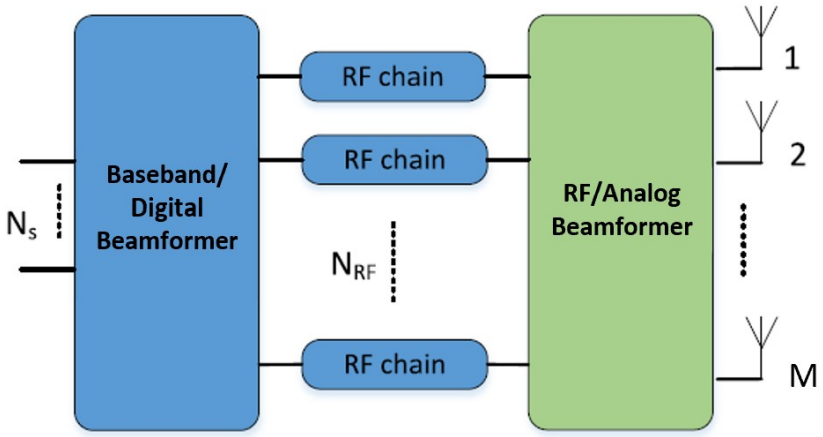

Figure 1.1: Hybrid Beamformer

Hybrid beamforming utilizes digital precoding for the initial signal processing at the baseband and then employs an analog beam-forming network at RF to establish the beam's shape and direction mostly based on phased array processing as shown in Fig 1.1. Phased arrays are capable of directing beams dynamically without moving the antennas physically, simply by adjusting the phase of signals across the antenna elements [8]. This adjustment leads to patterns of constructive and destructive interference, focusing energy in desired directions and improving power efficiency, signal quality, and communication range. This type of beamforming can be referred to as Maximum Directivity Beamforming (MDBF) as

it aims at only providing maximum power to the target user.

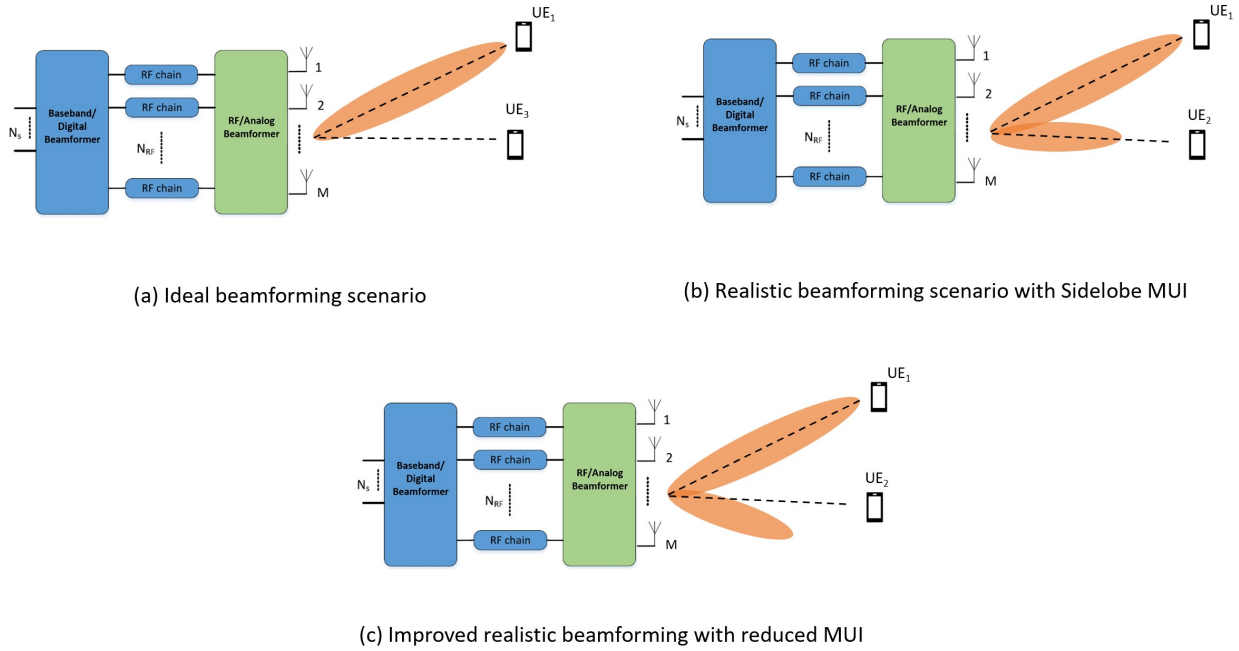

Figure 1.2: MUI challenge in HBF with target user UE_1

In HBF for MU-mMIMO systems, the main objective is to create highly directional and agile beams that serve multiple users simultaneously, while minimizing interference and maximizing intended signal quality. Ideally, beamforming should produce a narrow, precise beam that can be steered towards each target user, as illustrated in Fig. 1.2(a). This targeted beam effectively focuses energy, enhancing the signal-to-noise ratio (SNR) and improving system throughput. In an ideal case, there would be no radiation outside the main beam, meaning zero sidelobes and backlobes, allowing complete rejection of out-of-beam interferers and minimizing the interference between users. However, in practice, achieving such an ideal beam is impossible due to inherent limitations in the radiation characteristics of the array.

The presence of non-zero sidelobes and backlobes in the radiation pattern causes energy leakage beyond the main beam, resulting in Multi-User Interference (MUI). This interference occurs when signals intended for one user overlap and interfere with those for other users, as illustrated in Fig. 1.2(b). Such overlap reduces the SINR, thereby degrading overall system

performance. MUI becomes particularly problematic when multiple beams are formed using different sub-arrays at the same base station (BS). The close spatial proximity of these beams increases the risk of cross-talk between users leading to a degradation in communication quality.

Another significant challenge in practical implementations is the non-uniformity of the ERPs across the antenna array. Variations in ERPs arise from differences in physical characteristics, mutual coupling between elements, and environmental factors, resulting in beam distortion. This makes precise control over beam radiation and effective interference suppression more challenging. Such non-uniform radiation patterns exacerbate MUI, as sidelobes from each sub-array may inadvertently direct energy toward unintended users.

To mitigate MUI, it is essential to generate a beam radiation pattern that directs minimal energy towards unintended users, as shown in Fig. 1.2(c). Techniques that allow this are known as NCB methods, which aim to steer nulls (areas of very low or zero radiation) toward the interfering users, thereby reducing signal overlap and improving the SINR. NCB methods rely on knowledge of the target and interfering users' locations to strategically adjust the magnitudes and phase shifts of the signals fed to the antenna array. Essentially, NCB acts as a spatial filter, maximizing beam gain in the desired user directions while minimizing radiation power in directions where interference is likely. However, NCB methods still face the challenges posed by non-identical ERPs, which can make them less effective in practice, especially in dynamic environments involving many users.

This thesis aims to investigate a method to generate more effective beamforming radiation patterns in the presence of varying ERP. By examining the key role of Array Factor (AF) in array processing and the principles of the widely used NCB method, particularly the LCMV technique, the thesis identifies the limitations of the LCMV method when applied to real-world scenarios with heterogeneous antenna elements. Using measured antenna ERPs to represent the realistic antenna ERPs, the study highlights the drawbacks of applying LCMV under practical scenarios with non-uniform ERP.

A perturbation-based NCB method is then proposed, integrating the measured ERPs into the LCMV approach to generate the initial beamforming vector. This method employs a metaheuristic exploratory algorithm PSO, to further enhance the nulling performance. The approach effectively optimizes beamforming coefficients in MU-mMIMO systems, addressing the challenges of non-ideal and varying radiation patterns. The proposed solution provides

near-optimal results in both simulation and experimental testing, successfully minimizing interference while maximizing beamforming efficiency and overall system capacity.

The rest of the thesis is organized as follows: Chapter 2 provides the background on array processing and presents a detailed literature review of the current state-of-the-art NCB techniques, along with an explanation of the working principles of LCMV and related methods. Chapter 3 explores the challenges faced by LCMV in scenarios involving heterogeneous ERPs and evaluates its performance under different ERP conditions. Chapter 4 introduces the perturbation-based NCB method, explaining its core principles and presenting a comparative performance analysis against LCMV through both simulations and experimental testing. Additionally, it examines the impact of quantization on beamforming radiation patterns due to the limited resolution of practical phase shifters and attenuators. Finally, Chapter 5 provides the conclusion and outlines potential future research directions.

Chapter 2

Phased Array and Rx Beamforming

This chapter investigates Rx beamforming in phased array systems, focusing on conventional array processing techniques. It covers MDBF and examines the role of AF in beam shaping. Additionally, the chapter provides a literature review of existing NCB methods, with a detailed analysis of LCMV and related techniques.

2.1 Uniform Linear Antenna Array and Rx Beamforming

Beamforming involves the synthesis of radiation beams through the combination of outputs from multiple antenna elements, arranged according to a specific geometry. This technique allows dynamic adjustment of the beam direction to meet varying operational requirements. By applying calculated beamforming coefficients to these elements, an antenna array can achieve precise control over its beamforming characteristics. Each antenna element in the array has its own unique ERP that can influence the focusing and directing of the radiated power. By focusing this radiated power towards a specified target direction, the efficiency and effectiveness of communication in both transmit (Tx) and receive (Rx) modes can be improved.

As the beamforming capability of an antenna array is mainly determined by the number of antenna elements in that direction, this chapter will consider a $1 \times M$ Rx Uniform Linear Array (ULA) positioned along the x-axis, with elements uniformly spaced by a distance d.

The array is designed to receive signals from a Tx user located at a distance D from the array origin at the position of the first antenna element. In this thesis, the focus is on the far-field operation region, where D exceeds the Rayleigh Distance D_r. The D_r represents the boundary between the near field and far field regions and can be expressed as [8]:

$$D_r = \frac{2((M-1)d)^2}{\lambda_0}, \tag{2.1}$$

where λ_0 is the wavelength of the signal.

When the condition $D > D_r$ is met, the incoming wavefront can be approximated as planar by the time it reaches the array. This approximation holds because, at such distances, the curvature of the spherical wavefront originating from the source becomes negligible compared to the array's dimensions. As a result, the signals arriving on different elements of the array will appear to have nearly parallel paths. This allows us to treat the angle of arrival of the incoming signal as uniform across the array.

Figure 2.1(a) illustrates the position of a Tx User located in the far-field. The shaded area represents the plane of the Tx user, which can be defined by the line source of length D, azimuth angle θ on xy-plane and elevation angle ϕ between z-axis and line source.

Fig. 2.1(b) illustrates the propagation of the incoming signal in the xy plane. The pink dashed lines represent the projection of incoming rays from the target Tx user to the array antenna elements. The unit vector representing the direction of this dashed line is given by $\sin(\phi)$. The longest ray, originating from a distance D, reaches antenna element 0 and intersects the xy plane at the origin. Therefore, the length of this projected incoming ray is $D\sin(\phi)$.

Since the distance D is significantly larger than the array's aperture, the impact of the individual element positions on the magnitude of the incoming signal is negligible, allowing the assumption that all antenna elements receive the same signal power. However, due to the high carrier frequency f_c, even the smallest spacing between adjacent antenna elements can introduce a substantial phase difference between the signals received at each position. This phase difference, which depends on the Direction of Arrival (DoA) of the signal, must be accounted for during array processing to accurately reconstruct the incoming signal.

As shown in Fig. 2.1, the wavefronts that reach the antenna array are planar, represented

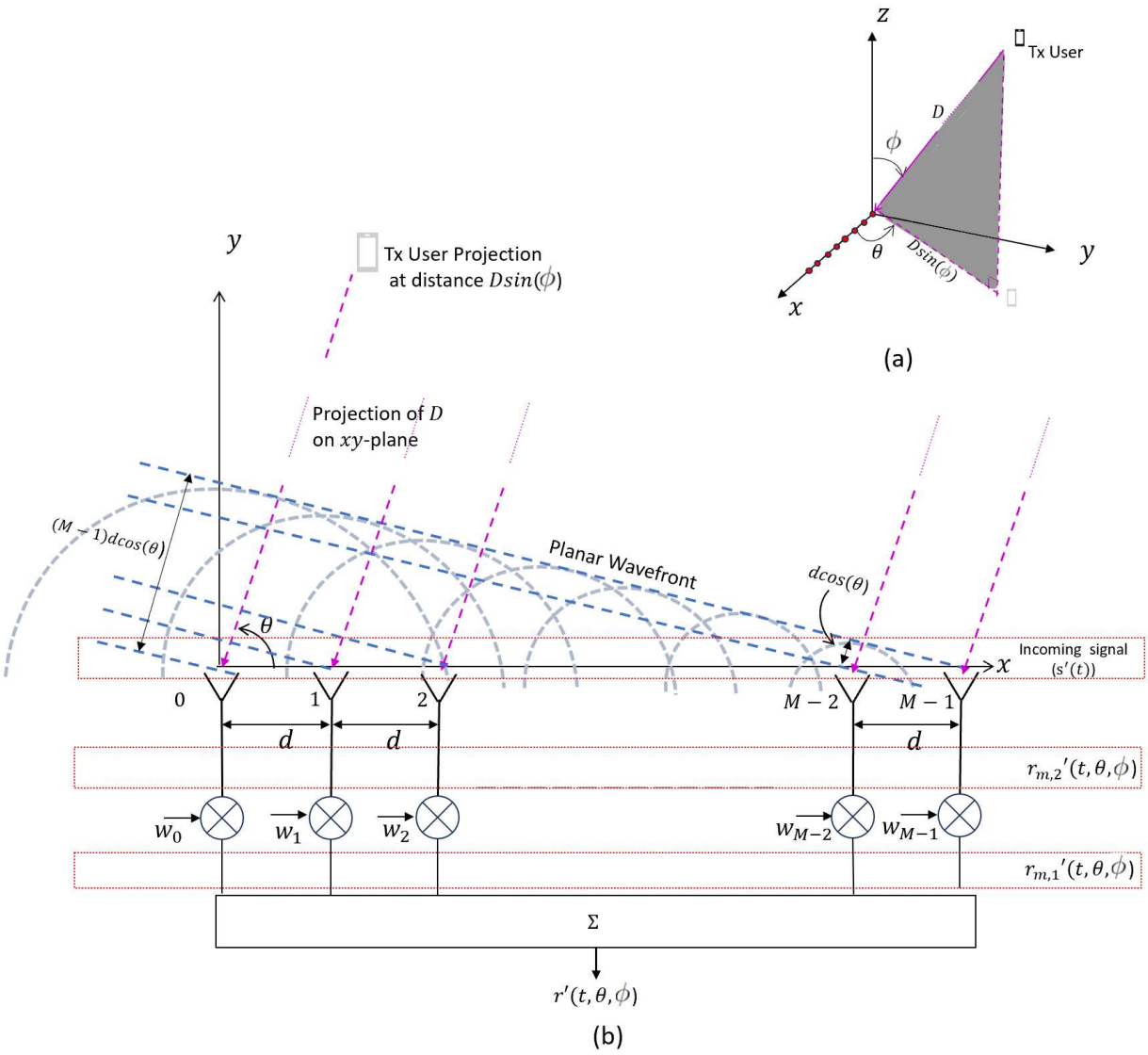

Figure 2.1: a) Location of Tx user relative to ULA. b) 2D xy-plane view

by blue dashed lines, resulting in identical signal delays between two consecutive antenna elements due to their uniform spacing. It can be observed that the projected ray length to the m^{th} element is shorter than that to the first element (denoted as $D\sin(\phi)$ for element 0) by $md\cos(\theta)$ for $m = 1, 2, \ldots, (M-1)$ in the azimuth plane. This decrement in projected

length implies a corresponding reduction in signal delay as the antenna index increases.

Considering the vector projection in three-dimensional space, the incoming signal's angular frequency $\omega_c = 2\pi f_c$ and propagation speed c in free space, the phase shift ζ resulting from the difference in signal delay can be written as

$$\begin{aligned}\zeta(\theta, \phi) &= \frac{\omega_c d \sin(\phi)\cos(\theta)}{c} \\ &= \beta d \sin(\phi)\cos(\theta),\end{aligned} \tag{2.2}$$

where $\beta = \frac{\omega_c}{c}$ is the phase constant of our signal representing phase change per unit distance.

Under the far-field assumption, each element in the antenna array receives a signal with uniform amplitude. However, the antenna element gains are heterogeneous and respond differently to the incoming wavefronts. This response is influenced by the ERP of each element and the spatial phase delays associated with their positions. As illustrated in Fig 2.1b, the actual modulated signal, $s'(t)$, is received by the phased array. This signal can be expressed as:

$$s'(t) = a(t)\cos(\omega_c t + \Phi(t)) = 0.5\left(s(t)e^{j\omega_c t} + s^*(t)e^{-j\omega_c t}\right), \tag{2.3}$$

where $a(t)$ represents the signal amplitude, $\Phi(t)$ is the phase shift and $s(t) = a(t)e^{j\Phi(t)}$ denotes the equivalent complex baseband signal of $s'(t)$.

The incoming signal received by the ULA undergoes modifications due to each antenna element's ERP and the phase delay introduced by the spatial positioning of the elements within the array. Consequently, the signal $r'_{m,2}(t, \theta, \phi)$ at the m^{th} antenna element can be modelled to account for these effects:

$$r'_{m,2}(t, \theta, \phi) = E_m(\theta, \phi)e^{jm\zeta(\theta,\phi)}s'(t) + n'_m(t), \tag{2.4}$$

where $E_m(\theta, \phi)$ denotes the normalized ERP for the m^{th} element in direction (θ, ϕ), and $n'_m(t) \sim \mathcal{CN}(0, \sigma_n^2)$ represents the Gaussian thermal noise at the m^{th} receiver.

In Rx beamforming, individual delays are adjusted to ensure the signal components are in-phase before summing. The beamforming coefficients, $w_m(\theta, \phi)$, are complex numbers that compensate for phase variations across the elements, enabling controlled constructive

and destructive summation of the received signals. These coefficients can be defined as:

$$\mathbf{w}(\theta,\phi) = [w_m(\theta,\phi) = W_m(\theta,\phi)e^{-jm\psi(\theta,\phi)}, m = 0,1,2,\ldots,(M-1)]^T, \tag{2.5}$$

where $\psi(\theta,\phi)$ is the phase compensation added by the coefficient and $W_m(\theta,\phi)$ adjusts the amplitude, helping to control sidelobe levels and steer nulls for interference rejection. In the case of constant-modulus, $W_m(\theta,\phi)$ is set to unity, representing isotropic ERP for each antenna element. The signal $r'_{m,1}(t,\theta,\phi)$, in Fig. 2.1, represents the signal in (2.4) once it has been updated with the beamforming coefficient. It can be modelled as:

$$r'_{m,1}(t,\theta,\phi) = w^*_m(\theta,\phi)E_m(\theta,\phi)e^{jm\zeta(\theta,\phi)}s'(t) + w^*_m(\theta,\phi)n'_m(t). \tag{2.6}$$

The final modulated received signal, $r'(t,\theta,\phi)$, is the output of the summation of all antenna responses:

$$r'(t,\theta,\phi) = \sum_{m=0}^{M-1}\left[w^*_m(\theta,\phi)E_m(\theta,\phi)e^{jm\zeta(\theta,\phi)}s'(t) + w^*_m(\theta,\phi)n'_m(t)\right]. \tag{2.7}$$

For convenience, in the subsequent discussions of this thesis, the focus will be on the equivalent baseband signal of the received signal, which can be expressed as follows based on (2.3).

$$\begin{aligned} r(t,\theta,\phi) &= \sum_{m=0}^{M-1}\left[w^*_m(\theta,\phi)(E_m(\theta,\phi)e^{jm\zeta(\theta,\phi)}s(t) + n_m(t))\right] \\ &= \mathbf{w}^H(\theta,\phi)\mathbf{a}(\theta,\phi)s(t) + \mathbf{w}^H(\theta,\phi)\mathbf{n}(t,\theta,\phi), \end{aligned} \tag{2.8}$$

where $\mathbf{a}(\theta,\phi)$, known as the steering vector, encapsulates the configuration of the antenna array, the ERPs, and the locations of the users:

$$\mathbf{a}(\theta,\phi) = \begin{bmatrix} 1 \\ E_1(\theta,\phi)e^{j\zeta(\theta,\phi)} \\ \vdots \\ E_{M-1}(\theta,\phi)e^{j(M-1)\zeta(\theta,\phi)} \end{bmatrix}. \tag{2.9}$$

In (2.8), the first term represents the desired signal, while the second term accounts for

the output noise, with $\mathbf{n}(t) = [n_m(t), m = 0, 1, 2, \ldots, (M-1)]^T$ as the complex-valued noise vector.

In the case of homogeneous ERP, which means that all antenna elements in the array exhibit identical ERPs such that $E_m(\theta, \phi) = E(\theta, \phi)$, the radiation pattern can be factored out of steering and noise vectors in (2.8):

$$r(t, \theta, \phi) = E(\theta, \phi)A(\theta, \phi)s(t) + E(\theta, \phi)\mathbf{w}^H(\theta, \phi)\mathbf{n}(t, \theta, \phi), \tag{2.10}$$

where $E(\theta, \phi) = 1$ for isotropic antenna elements and $A(\theta, \phi)$ is called the Array Factor (AF), which can be represented as:

$$A(\theta, \phi) = \sum_{m=0}^{M-1} \left[W_m(\theta, \phi) e^{jm[\zeta(\theta,\phi)+\psi(\theta,\phi)]} \right]. \tag{2.11}$$

2.2 Importance of Array Factor under MU scenario

A MU scenario presents a more complex and realistic challenge compared to the single-user case. In single-user scenarios, the system is focused solely on optimizing performance for one user, which simplifies the beamforming and signal processing tasks. However, this approach does not account for the need to manage multiple connections simultaneously without interference, as required in modern communication systems such as cellular networks, Wi-Fi, and satellite communications.

In a MU beamforming scenario, large-scale antenna arrays in mMIMO systems are deployed to efficiently serve multiple users simultaneously within the same frequency band, significantly enhancing network capacity and spectral efficiency. Through advanced signal processing techniques, these large-scale antenna arrays generate multiple beams, each directed toward a specific user, allowing for spatial multiplexing and optimal resource utilization.

However, this scenario introduces the critical challenge of managing MUI. Unlike single-user scenarios, where beamforming is solely focused on optimizing the signal to a single target, MU scenarios involve multiple users sharing the same communication resources, such as frequency bands, time slots, or spatial channels, leading to inevitable inter-user interference. This interference occurs when signals intended for different users

overlap and create cross-talk, which can significantly degrade communication quality.

Managing MUI becomes complex, as the beamforming process must achieve a dual objective: it must direct the main lobe with high gain toward the intended user while simultaneously minimizing side and back lobes that could interfere with other users. The challenge lies in maintaining a high SINR for all users, ensuring that each beam is sharp and precise enough to prevent energy leakage that contributes to MUI. Advanced beamforming algorithms and interference suppression techniques are crucial to handle these complexities and maintain high-quality communication in densely populated user environments.

The AF of the antenna array describes how the geometry and configuration of the antenna elements influence the radiation pattern. Acting as a spatial filter [8, 9], the AF is directly influenced by the number of antenna elements, the inter-element spacing, and the beamforming weights. In the MU scenario, these factors can be altered to change the radiation pattern of the antenna array to enhance signals from desired directions while suppressing those from undesired directions. This selective enhancement and suppression is analogous to a filter that allows certain frequencies to pass while attenuating others.

For constant-modulus beamforming coefficients (i.e. $W_m(\theta, \phi) = 1$) the AF from (2.11) simplifies to:

$$A(\theta, \phi) = \sum_{m=0}^{M-1} \left[e^{jm(\zeta(\theta,\phi)+\psi(\theta,\phi))} \right] = \sum_{m=0}^{M-1} \left[e^{jm\Psi(\theta,\phi)} \right], \tag{2.12}$$

where $\Psi(\theta, \phi) = \zeta(\theta, \phi) + \psi(\theta, \phi)$. The right-hand-side of (2.12) represents the sum of a finite geometric series with the common ratio $e^{j\Psi}$, which can also be written as:

$$\begin{aligned} A(\theta, \phi) &= \frac{(e^{jM\Psi} - 1)}{(e^{j\Psi} - 1)} \\ &= e^{j[(M-1)/2]\Psi} \left[\frac{e^{j(M/2)\Psi} - e^{-j(M/2)\Psi}}{e^{j(1/2)\Psi} - e^{-j(1/2)\Psi}} \right] \\ &= e^{j[(M-1)/2]\Psi} \left[\frac{sin(\frac{M}{2}\Psi)}{sin(\frac{1}{2}\Psi)} \right]. \end{aligned} \tag{2.13}$$

The closed form of AF in (2.13) shows its beam pattern would consist of a main lobe

and multiple sidelobes with the maximum directivity at $\Psi = 0$. The conventional MDBF technique operates on the principle of maximizing the power delivered to the target user in the desired direction (θ_i, ϕ_i). This can be accomplished by steering the beamforming coefficient's phase shift to counterbalance the spatial delay, i.e.,

$$\psi(\theta_i, \phi_i) = -\zeta(\theta_i, \phi_i). \tag{2.14}$$

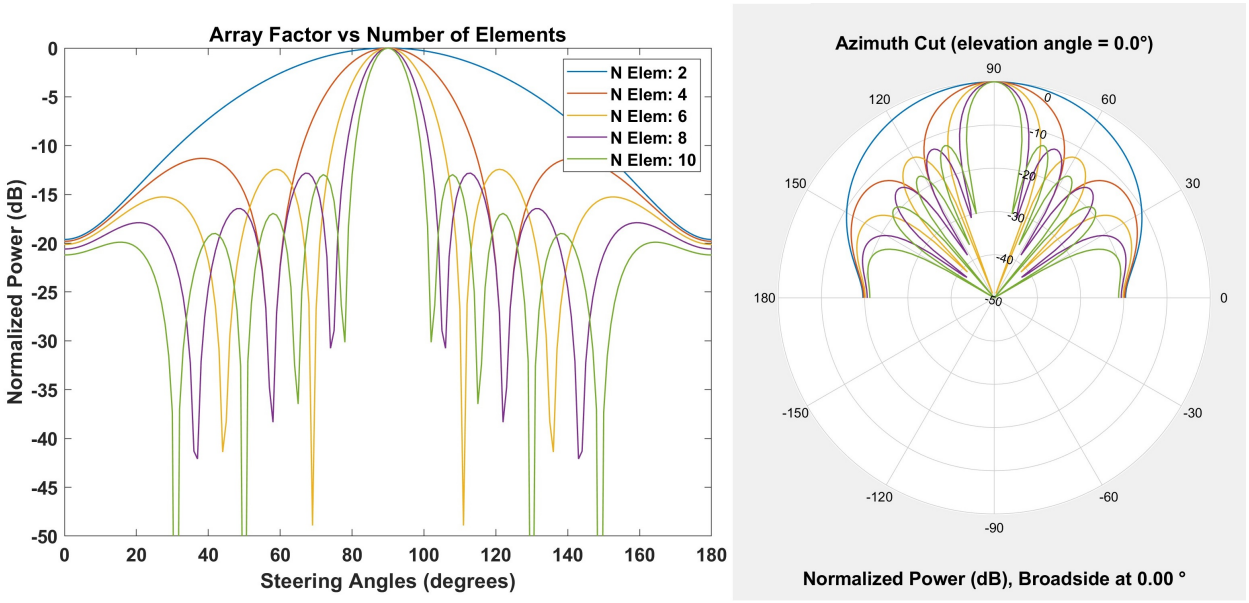

Figure 2.2: Array Factor vs Number of Antenna Elements (M)

To understand the impact of adjustments in the AF on the overall beam pattern, AF was plotted as a function of the number of elements in Fig. 2.2. This figure shows the 2D azimuth cuts of radiation patterns in both rectangular and polar coordinate systems. It illustrates the AF of phased arrays of varying sizes, maintaining consistent antenna spacing, and directing the main beam towards $\theta = 90°$ under the assumption of constant modulus beamforming coefficients $(W_m(\theta, \phi) = 1)$.

The plots show that increasing the number of antenna elements results in narrower First Null Beamwidth (FNBW) and slightly lower sidelobe levels. While larger arrays generate more sidelobes, their power is reduced compared to smaller arrays. Thus, larger

arrays provide improved beam focus and sidelobe suppression, but at the expense of higher equipment and power costs.

These sidelobes, representing energy not directed toward the main lobe's intended target, can cause MUI. This phenomenon is particularly problematic when different users share the same frequency, as the sidelobes of one receiving subarray may intercept signals intended for another.

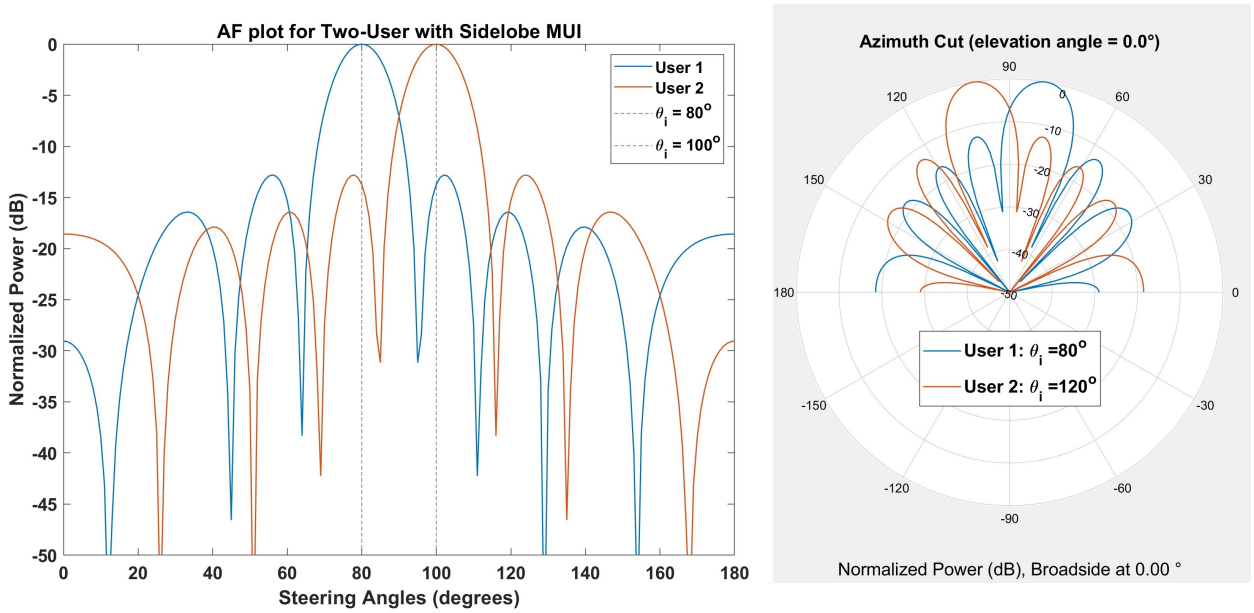

Figure 2.3: AF plots in Two-User Scenario

A visual representation of such a scenario is presented in Fig. 2.3. The setup features two 8-element subarrays operating simultaneously on the same beamwidth, aimed at serving users located in the directions of $\theta_i = 80°$ and $\theta_i = 100°$. The AF of both subarrays are plotted in Fig. 2.3, revealing that the sidelobes from each array are directed towards the unintended user, resulting in the reception of unwanted signals. Such overlapping leads to MUI, which can corrupt the communicated signals and induce significant communication challenges.

Minimizing the presence of high sidelobes in unintended directions is crucial for designing effective beamforming strategies. To achieve this, it is essential to determine

optimal beamforming coefficients that, unlike MDBF, not only maximize directivity but also reduce the MUI by reducing the sidelobe levels.

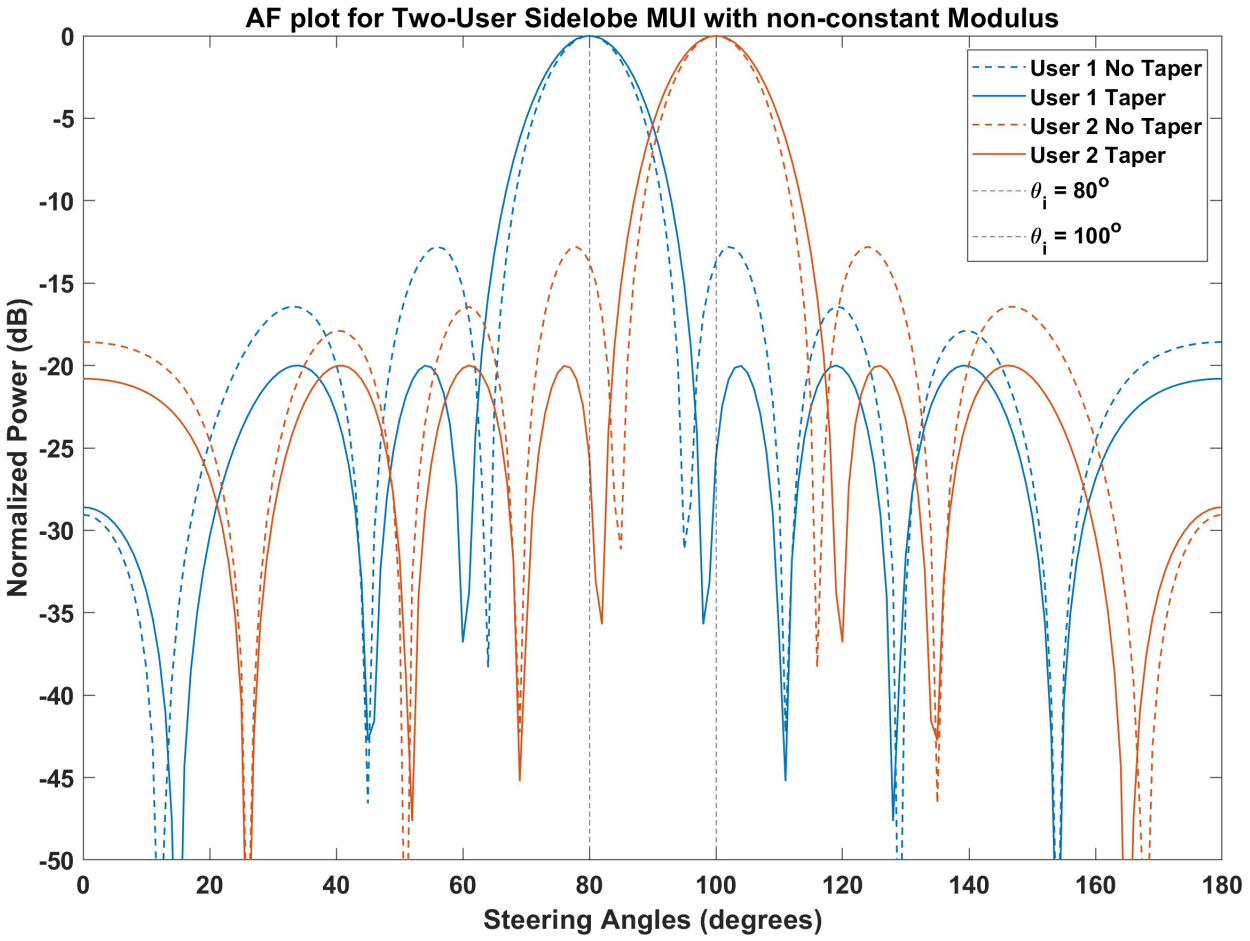

Figure 2.4: AF plots vs steering angles for Two-User MUI with Non-Constant Modulus beamforming coefficient

To examine how carefully selecting beamforming coefficients can affect the sidelobe levels, the assumption of constant modulus for our coefficient magnitudes was relaxed. Using the MATLAB Toolbox, simple tapering was applied to the beamforming coefficients and its impact was analyzed in a two-user scenario. Tapering allows the application of a windowing function to the beamforming coefficient magnitudes, resulting in non-uniform weights across

the antenna elements. The tapering is performed using a Chebyshev window, and the results are displayed in Fig. 2.4.

As can be observed, the non-constant modulus approach effectively reduces sidelobe levels, which helps to minimize MUI. However, this improvement comes with a tradeoff: an increase in the FNBW, leading to potential power wastage and additional interference for nearby users. On the positive side, the increase in FNBW highlights that beamforming coefficients can be adjusted to reposition the nulls as required. This flexibility is leveraged in advanced NCB techniques, where radiation nulls are strategically directed toward interfering users, further mitigating MUI.

The following sections will explore these techniques in detail to identify the most effective methods for optimizing beamforming coefficients. By carefully managing sidelobe levels and employing advanced beamforming strategies, system capacity can be significantly improved through minimized interference. This optimization enables denser user and channel packing, ensuring more reliable communications, particularly in environments where multiple subarrays operate simultaneously without causing performance degradation.

2.3 Nulling Control Rx Beamforming

2.3.1 Rx Beamforming

For power-efficient Rx operation, it is essential to minimize the power required for reliable communication. This involves designing the system to function effectively at low Rx signal power levels, close to the noise level while maintaining good detection performance. In multi-user environments, interference from other users can further complicate signal detection, as high sidelobes from adjacent transmissions can overlap with the desired signal, causing interference and reducing the effective SINR.

To overcome the challenges of maintaining high SINR while operating at low power levels, beamforming becomes an effective solution. By focusing energy in the desired direction, beamforming significantly improves SINR and reduces the impact of noise and interference. The most effective techniques for improving SINR and suppressing MUI, as part of NCB, direct the beam toward the desired user while simultaneously placing nulls in the radiation pattern toward interfering users, thereby reducing MUI.

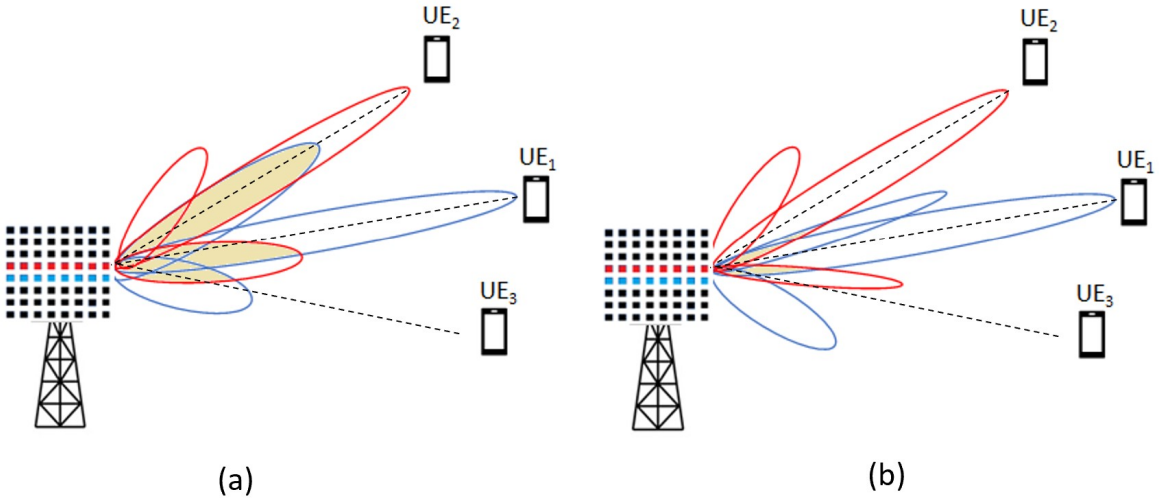

Figure 2.5: MU Beamforming comparison using multiple subarrays. a) MDBF Beamforming, b) Nulling Control Beamforming

Traditional beamforming techniques such as MDBF use a fixed set of pre-calculated weights to direct the beam in a predefined direction. This could lead to high MUI when signals from multiple subarrays operating at the same frequency overlap as shown by the shaded region in Fig. 2.5(a). This could lead to receiving unintended signals causing signal distortion or crosstalk during communication.

NCB techniques, which are part of Adaptive Beamforming (ABF), aim to enhance the performance of multi-user communication by dynamically adjusting the beam's radiation pattern in real-time based on the user's location. This trait allows the beamformer to focus on a specific target user in a dynamic environment while suppressing interference to other users by adjusting the beam radiation pattern. This adjustment maintains the main beam toward the intended user while nulls are placed in the directions of the unintended user (Fig. 2.5(b)).

This ability to generate deep and accurate nulls is crucial in multi-user operations, leading to improved SINR and overall system performance. The dual characteristic of NCB not only improves signal quality for the target user but also effectively mitigates MUI from other

users, as represented by the reduced shaded regions in Fig. 2.5(b). Additionally, placing nulls in the radiation pattern increases the system capacity, enabling communication with a higher number of users simultaneously using the same frequency through different subarrays.

Various NCB techniques have been studied and implemented which can be broadly divided into two categories: Non-iterative and Iterative. Non-iterative beamforming optimizes the beamforming weights based on direct calculations, leveraging the knowledge of both desired and interference signals, e.g., the covariance matrix of desired and interference signals. The beamforming weights are then directly computed by inverting the covariance matrix, which decorrelates the interference from the desired signal. A key advantage of non-iterative techniques lies in their speed, as the beamforming weights can be determined in a single step.

A non-iterative ABF algorithm, introduced in [10], uses real-valued coefficients with a ULA framework, employing a preprocessing transformation matrix. This algorithm, designed to either minimize mean square error (MSE) or maximize SINR, significantly reduces computational complexity and accelerates convergence. The technique presented in [11] treats null steering as a sparse recovery problem, using compressed sensing (CS) to perturb minimal elements and generate wide nulls, improving interference suppression by 10 to 20 dB while reducing hardware complexity.

The work in [12] presents the least mean square - least mean square (LLMS) algorithm, featuring dual LMS components, outperforming traditional LMS algorithms and others in terms of convergence efficiency and robustness against the additive white Gaussian noise (AWGN). In [13], authors introduce the RLS-CMA, a modified constant-modulus algorithm (CMA) utilizing Recursive Least Squares (RLS) for blind adaptive signal separation, achieving quicker convergence and superior tracking compared to existing methods.

Accurate performance of these non-iterative beamformers relies on the precise estimation of the steering vector $\boldsymbol{a}(\theta, \phi)$ and the noise covariance matrix $\mathbf{R}$. Algorithms such as LMS, Minimum Variance Distortionless Response (MVDR) [14–19], eigenvector decomposition (EVD) beamformer [20], diagonal loading beamformer [21–23], and LCMV [24–27] also depend on accurate channel statistics estimation.

While the deterministic beamforming approach facilitates the swift computation of beamforming vectors, it often yields suboptimal beamformers that exhibit insufficiently deep radiation nulls and inaccuracies in nulling angles under practical conditions. Factors

such as inter-element mutual coupling, non-uniformities among adjacent antenna elements, and asymmetries in the dielectric substrate and ground plane contribute to these variations. These discrepancies compromise the accuracy of the estimated array response [17], leading to a potential misalignment between the anticipated and actual spatial signal characteristics, thus degrading the precision of beam formation.

Moreover, non-uniform ERPs cause the beamforming vector to have varying effects on different array elements depending on the direction, leading to distortions in the beam radiation patterns. The simulations presented in [10–16, 24–26, 28, 29] typically assume isotropic or uniform ERPs, which do not accurately represent the diversity of ERPs in large antenna arrays. Factors such as element positioning, variations in element construction, asymmetries in the ground plane, and environmental conditions, as discussed in [1], significantly impact ERPs, thereby affecting the overall beamforming performance.

Iterative NCB techniques, unlike deterministic methods, use multiple iterations to refine beamforming weights based on specific optimization criteria. These methods offer higher precision and improved SINR by incrementally enhancing beamforming coefficients, effectively creating deeper nulls to mitigate MUI.

An iterative technique where beamforming coefficients are derived from the AF using Fourier Transforms is presented in [30]. This method significantly improves performance, speed, and flexibility by continually updating the coefficients until the desired pattern is achieved. The work presented in [31] employs Fast-Fourier Transformation (FFT) to generate wide nulls while minimizing sidelobe levels, demonstrating significant computational speed advantages.

In [32], the author presents a Bees Algorithm (BA) that searches for optimal amplitude values to place the null in the desired direction. The results presented show that BA is capable of forming single-, multiple-, and broad-band nulls to any prescribed directions by controlling the amplitude of each array element while also managing the maximum sidelobe levels.

Optimization algorithms like PSO and Genetic Algorithm (GA) are commonly used in iterative beamforming. For example, [33] details a PSO-based algorithm for sidelobe suppression and null placement by optimizing the array geometry and the magnitude and phase of the elements' feedings. Whereas, [34] introduces Comprehensive Learning Particle Swarm Optimizer (CLPSO) for synthesizing unequally spaced linear arrays with sidelobe

suppression, constrained beamwidth, and nulling control.

Similarly, the technique presented in [35] integrates GA with the Schelkunoff nulling technique for efficient beam steering and null placement in circular antenna arrays with fewer elements. Another GA-based method in [36] optimizes element positions to reduce power at null locations while stabilizing the main beam, demonstrating improved accuracy in null placement and depth. Simulation results confirm its effectiveness in suppressing interference in wireless systems.

In the literature on optimization techniques for wireless communications, PSO has been extensively compared to the GA in various studies. For example, [37] evaluates the performance of PSO and GA in phased array synthesis under three different configurations of steering weights: amplitude-only, phase-only, and complex. The results show that PSO explores the problem's hyperspace more effectively than GA, often yielding better solutions with lower computational complexity. Similarly, [38] compares GA and PSO in the context of horn antenna design, concluding that PSO outperforms GA, and that a hybrid PSO-GA algorithm delivers the best optimization performance in these scenarios.

Relevant studies have also demonstrated the superior capability of PSO in optimizing ABF weights. In [39], the PSO algorithm is applied to optimize phase-only weights in a linear antenna array for NCB under a two-user scenario, assuming isotropic antenna elements. When compared with GA, results from 1000 experimental runs show that PSO consistently produces more stable and superior radiation patterns. Furthermore, PSO required fewer evaluations of the fitness function, which is typically computationally expensive, indicating a clear performance advantage. Similarly, [40] compares PSO with the Dynamic Mutated Artificial Immune System (DM-AIS) and the Gravitational Search Algorithm (GSA) for optimizing NCB coefficients. The study concludes that PSO not only matches but frequently surpasses these more complex optimization techniques, significantly boosting SINR while making only minor adjustments to the beam shape. This further underscores the suitability of PSO for beamforming optimization in wireless communications, as it balances performance improvements with manageable computational overhead.

Additionally, [41] provides a comparative analysis between the Bacteria-Foraging Algorithm (BFA) and PSO for optimizing antenna arrays. The study examines the performance of both algorithms in tasks such as null steering and sidelobe suppression. The findings indicate that PSO outperforms BFA in null-steering tasks, while BFA exhibits

better performance in sidelobe suppression. This highlights the versatility of PSO in addressing critical beamforming challenges, especially in managing interference suppression through precise null placement.

In conclusion, the body of literature presents PSO as a highly effective optimization method for beamforming tasks, consistently demonstrating superior performance compared to GA, BFA, and other advanced algorithms. Its ability to optimize with fewer iterations and lower computational complexity, while achieving robust nulling and improved SINR, makes it the leading candidate to implement in our work.

Iterative methods do also face challenges such as convergence speed, computational complexity, and robustness against measurement inaccuracies. Ensuring quick adaptation to dynamic environments, manageable computational demands, and resilience to DoA estimation errors is crucial for effective performance. Integrating measured ERPs and validating these approaches experimentally is essential to bridge the gap between theoretical models and practical applications, optimizing NCB for real-world use. Further research is needed to explore realistic ERP variations and experimentally validate NCB techniques in practical scenarios, particularly in networks with quantized phase shifters and attenuators, to ensure robust interference mitigation.

Challenges for NCB

In practical scenarios, the DoA of the desired signal (θ_i, ϕ_i) or interference signals can change dynamically. Consequently, the feeding weights must be recalculated whenever such changes occur. As a result, NCB algorithms may not be efficient if the time to achieve an optimal solution exceeds the coherence time of the system.

The coherence time, in the context of NCB algorithms, refers to the duration over which the wireless channel remains relatively static. During this period, channel characteristics such as path loss, fading, and phase shift do not vary significantly, allowing the beamforming weights to remain effective. If the channel changes faster than the algorithm can adapt (i.e., if the coherence time is shorter than the adaptation time), beamformer performance can degrade.

For non-iterative NCB techniques, the design of pilot signals for channel estimation must consider coherence time to ensure accuracy. In iterative NCB techniques, it is crucial that the system converges to an optimal solution within the coherence time; otherwise, the solution

will be ineffective due to changing system conditions.

2.3.2 LCMV Nulling Control Beamforming

The LCMV algorithm is a traditional non-iterative NCB technique that minimizes noise power (variance) while adhering to multiple linear constraints. This flexibility allows it to adapt to various scenarios by preserving signal quality in specific directions and attenuating undesired signals, making it suitable for our MU system assumptions.

The LCMV beamformer for the Rx ULA is formulated by defining the noise covariance matrix, specifying the linear constraints, and setting the objective function to minimize noise power. In this thesis, it is assumed that the system's coherence time exceeds the adaptation time required by the LCMV algorithm, the perturbation-based optimization method, and the supervised learning method.

LCMV Beamformer

The incoming signal vector on the isotropic M-element ULA from the main user direction (θ, ϕ) is given by (2.8). This can be rewritten as the following equation:

$$\begin{aligned} r(t,\theta,\phi) &= \mathbf{w}^H(\theta,\phi)\left[\mathbf{a}(\theta,\phi)s(t) + \mathbf{n}(t,\theta,\phi)\right] \\ &= \underbrace{\mathbf{w}^H(\theta,\phi)\mathbf{a}(\theta,\phi)s(t)}_{\text{Desired Response}} + \underbrace{\mathbf{w}^H(\theta,\phi)\mathbf{n}(t,\theta,\phi)}_{\text{Noise Response}} \end{aligned} \tag{2.15}$$

where $s(t)$ is the incoming baseband signal, $\mathbf{w}^H(\theta,\phi) \in \mathbb{C}^{1\times M}$ is the Hermitian of the complex beamforming vector, $\mathbf{a}(\theta,\phi)$ is the steering vector and $\mathbf{n}(t,\theta,\phi) \in \mathbb{C}^{M\times 1}$ is a complex-valued noise vector.

It's important to note that in subsequent sections, the discrete-time model will be considered with its sampling time equal to the modulation symbol interval. Under the assumptions of coherent and synchronous detection/operation, the time index t can be omitted for simplicity. The complex-valued modulation symbol is denoted as s, which adheres to the power constraint $\mathbb{E}\{ss^H\} = 1$, and the sampled discrete complex noise vector as $\mathbf{n}(\theta,\phi)$.

When discussing the Rx beamformer, it is important to note that the operating Rx signal

power is often close to the noise power. Therefore, the interference from other users and the noise have comparative power levels and can be combined into a single $\mathbf{n}(\theta,\phi) \sim \mathcal{CN}(0,\mathbf{R})$ complex-valued noise vector having covariance matrix $\mathbf{R}$. This combined term simplifies the analysis and design of the beamforming algorithm. The combined noise power P_n can be expressed as:

$$\begin{aligned} P_n = E\{|\mathbf{w}^H(\theta,\phi)\mathbf{n}(\theta,\phi)|^2\} &= E\{\mathbf{w}^H(\theta,\phi)\mathbf{n}(\theta,\phi)\mathbf{n}^H(\theta,\phi)\mathbf{w}(\theta,\phi)\} \\ &= \mathbf{w}^H(\theta,\phi)E\{\mathbf{n}(\theta,\phi)\mathbf{n}^H(\theta,\phi)\}\mathbf{w}(\theta,\phi) \\ &= \mathbf{w}^H\mathbf{R}\mathbf{w}. \end{aligned} \tag{2.16}$$

The LCMV algorithm finds the optimal beamforming coefficients ($\mathbf{w}_{lcmv}$) that minimize the output power of the noise (P_n) subject to linear constraints. To define the constraints, let us assume that our subarray is transmitting in K_c directions (θ_j,ϕ_j) where $j = 1,2,3,\ldots,K_c$. Our desired direction is set as (θ_i,ϕ_i) and the rest of the directions as undesired, i.e., (θ_j,ϕ_j) where $j \neq i$. To ensure maximum SINR, the goal is to find the set of coefficients $(\mathbf{w}(\theta_i,\phi_i))$ that satisfy the constraint of maximum gain in the desired direction, i.e., $\mathbf{w}^H(\theta_i,\phi_i)\mathbf{a}(\theta_i,\phi_i)$, and the constraint of no gain in all other directions, i.e., $\mathbf{w}^H(\theta_i,\phi_i)\mathbf{a}(\theta_j,\phi_j) = 0$ where $j \neq i$. This leads to K_c linear constraints, which can then be written in a matrix form as

$$\mathbf{C}^H\mathbf{w} = \mathbf{g}, \tag{2.17}$$

where $\mathbf{C}$ is $M \times K_c$ matrix containing all the steering vectors towards all K_c users and $\mathbf{g}$ is the constraint gain column vector of size K_c. Then the optimization problem is written as

$$\min_{\mathbf{w}} \mathbf{w}^H\mathbf{R}\mathbf{w} \qquad \text{subject to } \mathbf{C}^H\mathbf{w} = \mathbf{g}. \tag{2.18}$$

Each column of the constraint matrix $\mathbf{C}$ defines the steering vector $\mathbf{a}(\theta,\phi)$ in the specific direction of the constraint. For clarity, the steering vector for the desired direction is typically placed in the first column and the steering vectors for the other constraints in the subsequent columns. This can be represented as:

$$\mathbf{C} = \left[\ \mathbf{a}(\theta_i,\phi_i)\ \vdots\ \mathbf{a}(\theta_2,\phi_2)\ \vdots\ \ldots\ \vdots\ \mathbf{a}(\theta_{K_c},\phi_{K_c})\ \right].$$

The corresponding gain vector is designed to put the constraint of maximum gain (unity) in the desired direction and no gain (e.g., 0) in the other directions, i.e.,

$$\mathbf{g} = \left[\begin{array}{c:c:c:c} 1 & 0 & ... & 0 \end{array}\right]^T.$$

To solve this optimization problem, the Lagrange multipliers method is employed as shown in [42, 43]. The Lagrangian equation for this problem can be formulated as:

$$\mathcal{L}(\mathbf{w}, \lambda) = \mathbf{w}^H \mathbf{R} \mathbf{w} - \lambda(\mathbf{w}^H \mathbf{C} - \mathbf{g}^T), \tag{2.19}$$

where λ is the Lagrange multiplier. To get the optimal coefficients, derivative of (2.19) is taken with respect to $\mathbf{w}^H$:

$$\frac{\partial \mathcal{L}}{\partial \mathbf{w}} = \mathbf{R}\mathbf{w} - \lambda \mathbf{C}.$$

The derivative is equated to zero to find the optimal weight $\mathbf{w}$:

$$\begin{aligned} \mathbf{R}\mathbf{w} - \lambda \mathbf{C} &= 0 \\ \mathbf{w} &= \lambda \mathbf{R}^{-1} \mathbf{C}. \end{aligned} \tag{2.20}$$

Inserting this value of $\mathbf{w}$ into constraint in (2.18) to find value of the Lagrange multiplier:

$$\begin{aligned} \mathbf{C}^H \mathbf{w} &= \mathbf{g}, \\ \lambda \mathbf{C}^H \mathbf{R}^{-1} \mathbf{C} &= \mathbf{g}, \\ \lambda &= \frac{\mathbf{g}}{\mathbf{C}^H \mathbf{R}^{-1} \mathbf{C}}. \end{aligned}$$

Finally substituting the value of λ in (2.20) to get optimized LCMV weights

$$\mathbf{w}_{lcmv} = \frac{\mathbf{R}^{-1}\mathbf{C}}{\mathbf{C}^H \mathbf{R}^{-1} \mathbf{C}} \mathbf{g} \tag{2.21}$$

In the case of uniform ERPs, the signal covariance matrix $\mathbf{R}$ accurately reflects the statistical properties of the signals received by the antenna array and is well-conditioned, with a smaller spread of eigenvalues. This results in a more symmetric and balanced matrix,

which is crucial for minimizing numerical errors and enhancing the stability of computations during matrix inversion, which is a critical step in the LCMV beamforming method as shown in (2.21). Uniform ERPs also lead to consistent and predictable beam patterns, allowing the LCMV algorithm to generate near-optimal beamforming weights that achieve deep nulls with high precision.

In contrast, non-uniform ERPs introduce significant variations in element responses, leading to a poorly conditioned covariance matrix. This poor conditioning makes matrix inversion more challenging and can result in suboptimal beamforming weights, inadequate interference suppression, and inaccuracies in nulling angles. Consequently, it is important to consider the impact of non-uniform ERPs on the overall performance of the LCMV beamformer, to be discussed in the following chapter.

Minimum Variance Distortionless Response (MVDR)

The MVDR beamformer, also known as the Capon beamformer [44, 45], is a specialized adaptation of the LCMV beamforming technique. It aims to minimize the noise power (or variance) at the beamformer output while ensuring that the signal from the desired direction achieves the maximum gain, hence maintaining a distortionless response (DR). In relation to LCMV, MVDR can be seen as a special case in which the constraint matrix $\mathbf{C}$ has only one column that defines the steering vector $\mathbf{a}(\theta_i, \phi_i)$ in the desired direction for maximum response. Consequently, the gain constraint vector $\mathbf{g}$ contains a single value of unity, underscoring the 'distortionless' nature of this approach.

The MVDR algorithm utilizes a similar strategy to LCMV for determining the optimal weight vector, $\mathbf{w}_{mvdr}$, with the objective of minimizing the output noise power P_n. The solution to this optimization process can be found by adapting the LCMV weight equation (2.21) with the specific constraints imposed by the MVDR framework: the constraint matrix is replaced with the steering vector and the constraint gain vector with unity, i.e.,

$$\mathbf{w}_{mvdr}(\theta_i, \phi_i) = \frac{\mathbf{R^{-1}a}(\theta_i, \phi_i)}{\mathbf{a}^H(\theta_i, \phi_i)\mathbf{R^{-1}a}(\theta_i, \phi_i)} \tag{2.22}$$

If the channel noise is considered to be AWGN, its covariance matrix is:

$$\mathbf{R} = \sigma^2\mathbf{I}$$

where σ^2 is the noise power and $\mathbf{I}$ is the identity matrix. In this context, the MVDR beamformer aims to minimize the variance of the output while maintaining a distortionless response in the desired direction. Substituting $\mathbf{R}^{-1} = \frac{1}{\sigma^2}\mathbf{I}$ into (2.22) to get:

$$\begin{aligned} \mathbf{w}_{mvdr} &= \frac{\frac{1}{\sigma^2}\mathbf{a}(\theta_i, \phi_i)}{\mathbf{a}^H(\theta_i, \phi_i)\frac{1}{\sigma^2}\mathbf{a}(\theta_i, \phi_i)} \\ &= \frac{\mathbf{a}(\theta_i, \phi_i)}{\mathbf{a}^H(\theta_i, \phi_i)\mathbf{a}(\theta_i, \phi_i)} \end{aligned} \tag{2.23}$$

This shows that if the channel noise is AWGN, the MVDR beamformer weights are simply the steering vector normalized by the inner product of the steering vector with itself (i.e. its power)

2.4 Concluding Remarks

In this chapter, a case of Rx beamforming was presented, introducing the NCB techniques of LCMV and MVDR under the assumption of an isotropic ULA. The goal was to provide a comprehensive understanding of the theoretical foundations, existing research, and the challenges these algorithms face in multi-user scenarios.

In the next chapter, the focus will shift to examining the performance of the LCMV algorithm in a more realistic scenario involving heterogeneous antenna elements. This investigation aims to identify the limitations LCMV may face in practical implementations, particularly in terms of precision and nulling levels. By uncovering these challenges, the potential performance degradation caused by non-uniform radiation patterns in a multi-user environment can be better understood.

The studies in the next chapter will serve as a baseline for further optimization efforts. In the subsequent chapters, a novel perturbation-based approach will be introduced to enhance the system's SINR. This method aims to address the identified limitations and improve the overall effectiveness of NCB techniques in real-world applications.

Chapter 3

LCMV-Based Tx beamforming with Heterogeneous Antenna Elements

In Tx beamforming for multiple users, each user is served by a distinct sub-array of the antenna array. However, the beam intended for one user can still cause interference to others due to out-of-target radiation. Unlike Rx beamforming, Tx beamforming does not need to account for thermal noise, as the noise generated within the transmitter is negligible compared to the transmitted signal. As a result, for Tx beamforming, the focus can be entirely on efficiently directing signal power to the target user while minimizing interference to other users by controlling sidelobe radiation, ensuring optimal performance across multiple users.

In LCMV beamformer derivation, variations in ERP magnitude responses can result in a poorly conditioned signal covariance matrix with a wide eigenvalue distribution, undermining the numerical stability of matrix inversion during optimization. Computational errors in matrix inversion can cause significant numerical inaccuracies. This degrades the steering coefficients, impairing interference suppression and leading to discrepancies in nulling angles. As demonstrated in [1], larger ERP variations increase the degradation of nulling depth and angle accuracy. This chapter investigates the impact of non-uniform ERPs on the LCMV performance.

3.1 System Model

For our ABF approach, as shown in Fig. 3.1, consider the i^{th} M-element sub-array operating in an environment with K users, where $K < M$. The objective is to transmit the signal s_i to the desired user (UE_1) in the direction (θ_i, ϕ_i) while placing radiation nulls in the directions of the remaining $K-1$ unintended users (θ_j, ϕ_j) for $j \neq i$.

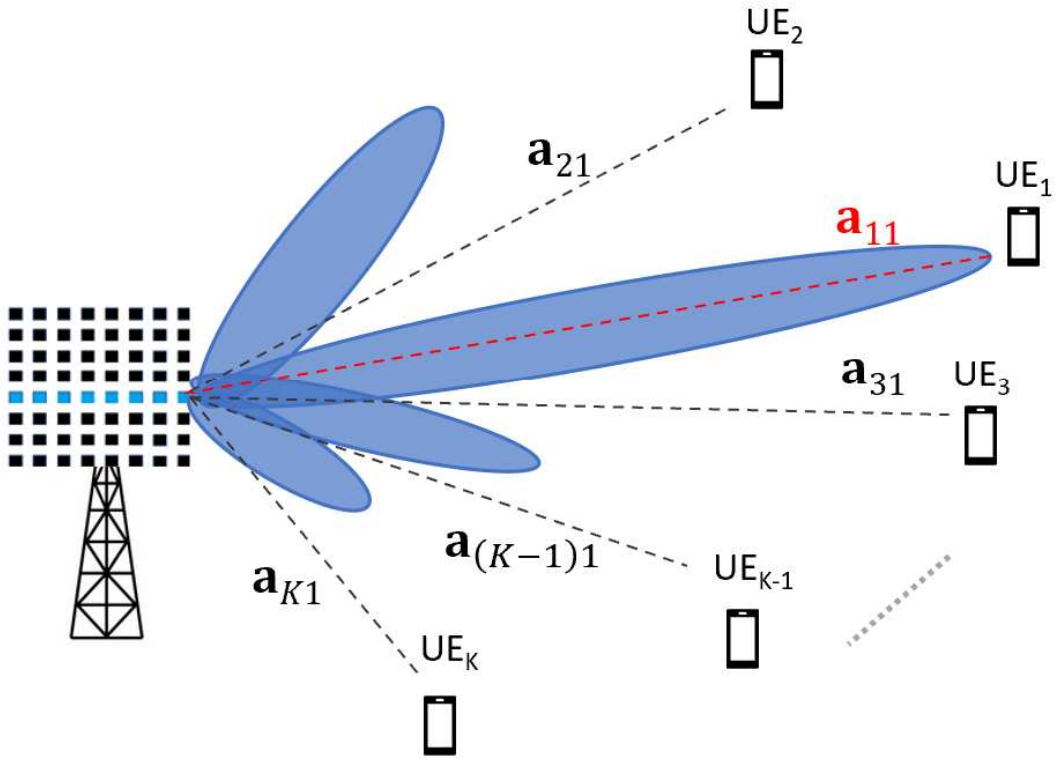

Figure 3.1: Tx Beamforming in desired user UE_1 direction, while mitigating interference to in other users' directions

The radiation pattern produced by the Tx beamforming phased sub-array, as shown in Fig. 3.1, consists of the desired signal transmitted to the target user and unintended signals causing interference to other users. The signal transmitted by the i^{th} subarray can be mathematically expressed as the sum of these components:

$$\boldsymbol{t}_i(\theta_i, \phi_i, \boldsymbol{\theta}_N, \boldsymbol{\phi}_N) = \underbrace{\mathbf{w}_i^H \mathbf{a}_i(\theta_i, \phi_i) s_i}_{\text{Desired Signal}} + \underbrace{\mathbf{w}_i^H \boldsymbol{\mathcal{A}}_i(\boldsymbol{\theta}_N, \boldsymbol{\phi}_N) s_i}_{\text{Interference}} \tag{3.1}$$

The first term denotes the i^{th} sub-array transmitting the intended signal towards the target user i, located in the direction (θ_i, ϕ_i). The symbol s_i represents the transmitted signal symbol from this subarray. The beamforming vector for i^{th} subarray, denoted by $\mathbf{w}_i \in \mathbb{C}^{M\times 1}$, controls the constructive and destructive summation of the transmitted signal at each antenna element giving shape and direction to the transmitted beam pattern. The vector $\mathbf{a}_i(\theta_i, \phi_i) \in \mathbb{C}^{M\times 1}$ represents the steering vector of the i^{th} subarray towards the intended user in direction (θ_i, ϕ_i) and is composed of antenna element positions, propagation directions, and antenna ERPs, as given in (2.9).

The second term in (3.1) represents the $K-1$ signals transmitted from the subarray to users other than the intended user i. The interference steering matrix $\boldsymbol{\mathcal{A}}_i(\boldsymbol{\theta}_N, \boldsymbol{\phi}_N) \in \mathbb{C}^{M\times(K-1)}$ maps the steering vectors towards the $K-1$ users from the i^{th} transmitter, which has M antenna elements. The $1 \times (K-1)$ angle vectors $\boldsymbol{\theta}_N = [\theta_1, ..., \theta_{(i-1)}, \theta_{(i+1)}, ..., \theta_K]$ and $\boldsymbol{\phi}_N = [\phi_1, ..., \phi_{(i-1)}, \phi_{(i+1)}, ..., \phi_K]$ represent the interference directions. Each column of $\boldsymbol{\mathcal{A}}_i(\boldsymbol{\theta}_N, \boldsymbol{\phi}_N)$ corresponds to a steering vector $\mathbf{a}_i(\theta_j, \phi_j)$, where j ranges from 1 to K, excluding i, i.e.,

$$\boldsymbol{\mathcal{A}}_i(\boldsymbol{\theta}_N, \boldsymbol{\phi}_N) = [\mathbf{a}_i(\theta_1, \phi_1), ..., \mathbf{a}_i(\theta_{i-1}, \phi_{i-1}), \mathbf{a}_i(\theta_{i+1}, \phi_{i+1}), ..., \mathbf{a}_i(\theta_K, \phi_K)]. \tag{3.2}$$

Unlike regular LCMV implementation which aims to minimize the output noise power, the modified optimization problem aims at properly designing the beamforming coefficient vector $\mathbf{w}_i$, to minimize the total output power towards unindented user directions, i.e., $\mathbf{w}_i^H \boldsymbol{\mathcal{A}}_i(\boldsymbol{\theta}_N, \boldsymbol{\phi}_N) s_i \approx 0$, while maintaining the strength of the desired signal in the intended user direction.

The power transmitted in the interference direction by the i^{th} transmitter is

$$\begin{aligned} E\{|\mathbf{w}_i^H \boldsymbol{\mathcal{A}}_i(\boldsymbol{\theta}_N, \boldsymbol{\phi}_N) s_i|^2\} &= E\{|s_i|^2\} E\{|\mathbf{w}_i^H \boldsymbol{\mathcal{A}}_i(\boldsymbol{\theta}_N, \boldsymbol{\phi}_N)|^2\} \\ &= E\{\mathbf{w}_i^H \boldsymbol{\mathcal{A}}_i(\boldsymbol{\theta}_N, \boldsymbol{\phi}_N) \boldsymbol{\mathcal{A}}_i^H(\boldsymbol{\theta}_N, \boldsymbol{\phi}_N) \mathbf{w}_i\} \\ &= \mathbf{w}_i^H E\{\boldsymbol{\mathcal{A}}_i(\boldsymbol{\theta}_N, \boldsymbol{\phi}_N) \boldsymbol{\mathcal{A}}_i^H(\boldsymbol{\theta}_N, \boldsymbol{\phi}_N)\} \mathbf{w}_i \\ &= \mathbf{w}_i^H \mathbf{R}_i(\boldsymbol{\theta}_N, \boldsymbol{\phi}_N) \mathbf{w}_i, \end{aligned} \tag{3.3}$$

where $\mathbf{R}_i(\boldsymbol{\theta}_N, \boldsymbol{\phi}_N)$ is the covariance matrix of $\boldsymbol{\mathcal{A}}_i(\boldsymbol{\theta}_N, \boldsymbol{\phi}_N)$. The diagonal elements of the matrix $\mathbf{R}_i(\boldsymbol{\theta}_N, \boldsymbol{\phi}_N)$ quantify the power of each undesired signal component from the corresponding antenna elements. The off-diagonal elements describe the correlations between these components across different elements.

Updating the LCMV optimization objective, defined in (2.18), the optimum coefficients can be achieved by minimizing the total transmitted interference power in (3.3) while maintaining the high power gain (g) in the intended user direction (θ_i, ϕ_i), i.e,

$$\min_{\boldsymbol{w_i}} \{\mathbf{w}_i^H \mathbf{R}_i(\boldsymbol{\theta}_N, \boldsymbol{\phi}_N) \mathbf{w}_i\} \qquad \text{conditional on } \mathbf{w}_i^H \mathbf{a}(\theta_i, \phi_i) = \sqrt{g}.$$

The solution to the updated objective function is derived using the Lagrange Multiplier method given in (2.19) to get:

$$\mathbf{w}_{lcmv}(\theta_i, \phi_i, \boldsymbol{\theta}_N, \boldsymbol{\phi}_N) = \sqrt{g} \frac{\mathbf{R}_i^{-1}(\boldsymbol{\theta}_N, \boldsymbol{\phi}_N) \mathbf{a}(\theta_i, \phi_i)}{\mathbf{a}^H(\theta_i, \phi_i) \mathbf{R}_i^{-1}(\boldsymbol{\theta}_N, \boldsymbol{\phi}_N) \mathbf{a}(\theta_i, \phi_i)}. \tag{3.4}$$

While the LCMV algorithm uses spatial filtering to preserve the intensity of the intended signal and reduce interference, its effectiveness critically depends on accurately aligning the array's response with the spatial characteristics of both desired and interfering signals. As outlined in (2.9) and (3.2), the desired signal steering vector $\mathbf{a}_i(\theta_i, \phi_i)$ and the interference steering matrix $\boldsymbol{\mathcal{A}}_i(\boldsymbol{\theta}_N, \boldsymbol{\phi}_N)$ are shaped by the ERPs of individual elements. As mentioned in Section 2.3.2, under the assumption of uniform ERP, it is easier to capture and predict the statistical properties of the desired and interfering signals, leading to a well-conditioned covariance matrix.

In the next section, multiple simulations will be used to observe the effects of non-uniform ERPs and how variations in ERPs impact the performance of LCMV. As horizontal linear phased arrays are used for beamforming, the beam's steerability will be confined to the azimuth plane. Therefore, for simplicity, all simulations and measurements will assume that users are located on the azimuth plane with a fixed elevation angle of $\phi = 90°$.

3.2 Illustrative Results

3.2.1 Element Pattern Measurement Setup

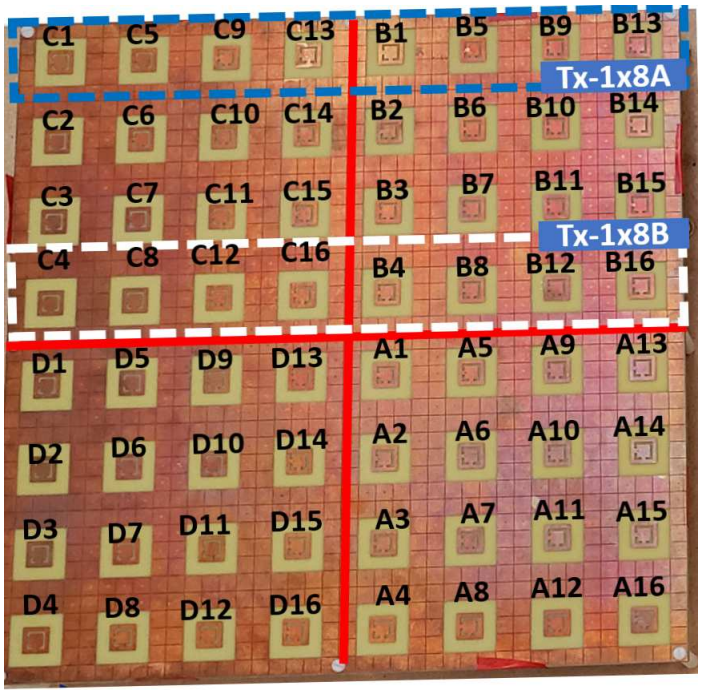

Figure 3.2: 8x8 antenna array prototype and element/sub-array indices.

In our experimental measurements of ERPs, we utilized an 8×8 dual-layer electromagnetic bandgap (EBG) array featuring circularly polarized (CP) patch antennas, designed for mMIMO systems and operating within the 3.35 GHz to 3.6 GHz frequency range, as shown in Fig. 3.2. To mitigate spatial aliasing in the beamforming process, the spacing between adjacent radiating patch elements was set to 2.78 cm ($0.32\lambda_0$ at 3.5 GHz)

edge-to-edge or 4.00 cm ($0.47\lambda_0$) center-to-center. This configuration achieved an isolation level better than 14.3 dB between neighbouring elements [46].

Measurements were performed in an anechoic chamber measuring 6.1 m × 2.4 m × 2.4 m (length × width × height) and fitted with C-RAM SFC-48 absorbers to minimize reflections and external interference. To streamline the measurement process, calibrated 1-to-16 RF switches, controlled by a custom Serial Peripheral Interface (SPI) module, were employed to enable sequential switching and measurement of each of the 16 elements in a set, with only one antenna element active during each measurement.

The NSI2000 platform, integrated with a vector network analyzer (VNA), was used to collect data. The ERPs were scanned with a resolution of 1° for both the θ and ϕ angles, with θ ranging from $-180°$ to $180°$ and ϕ from $-90°$ to $90°$. Measurements covered the operational frequency range from 3.35 GHz to 3.6 GHz, with a step size of 0.05 GHz. The normalized 3D radiation pattern for the m^{th} element at each frequency was stored in a matrix $\mathbf{E}_m \in \mathbb{R}^{361\times181}$, where each entry $E_m(\theta, \phi)$ represents the normalized radiation value at angle (θ, ϕ).

(a) Tx-1x8A

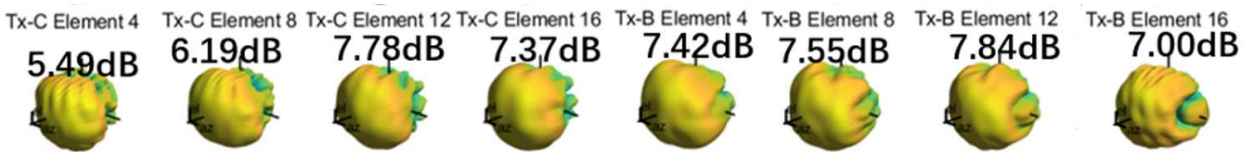

(b) Tx-1x8B

Figure 3.3: Tx-1x8 Element 3D-Radiation Patterns

The measurements reveal an average directivity of 6.95 dB across all elements. The measured ERPs, including directivity values for 16 key elements from two horizontal subarrays, highlighted in Fig. 3.2, are presented in Fig. 3.3. Edge elements in subarray Tx-1 × 8A, particularly those subject to strong inter-element mutual coupling along the x-axis, exhibited a slight reduction in directivity and increased distortion, as shown in

Fig. 3.3(a). In contrast, elements nearer the array's center, such as those in subarray Tx-1 × 8B, demonstrated more consistent radiation patterns, as illustrated in Fig. 3.3(b).

3.2.2 LCMV performance for Two-User case

To present the challenges caused by the varied ERPs on the LCMV beamforming process, we simulate its performance on a Tx sub-array using four distinct element pattern assumptions:

1. **Isotropic**: All elements are assumed to be isotropic.
2. **Homogeneous**: All elements are assumed to have the same radiation pattern, represented by the central element B4 of the Tx board, as shown in Fig. 3.2.
3. **Tx-1×8B**: Represents the center 1x8 sub-array with minimal radiation pattern variation, as shown in Fig. 3.3b.
4. **Tx-1×8A**: Represents the edge 1x8 sub-array with significant radiation pattern variation, as shown in Fig. 3.3a.

The simulation was conducted using MATLAB Phased Array Toolbox and built-in functions to calculate the LCMV and MDBF coefficients. The two-user scenario was considered, with the intended user located at θ_i and the unintended user at θ_N. The 16-sample simulation proceeded in two phases. In the first phase, 8 simulations were performed by varying the interference user angle (θ_N) within the range of $-30°$ to $30°$, while keeping θ_i fixed at $5°$. This allowed for the observation of how changes in the null location affected performance while the main user direction remained constant. The performance of LCMV was compared to the MDBF benchmark to evaluate SINR improvements, with the results presented in Table 3.1.

For isotropic and homogeneous radiation pattern configurations, the LCMV results for nulling depth surpass the MDBF condition by an average of -47 dB. The performance of both cases is identical, showing that LCMV generates optimal results if all antenna elements exhibit the same radiation pattern.

For the Tx-1×8B sub-array, LCMV's efficiency drops noticeably, with average null depths of -29.7 dB (37 dB worse than with isotropic sources) and showing an average improvement of only -9 dB over the MDBF scenario.

	Normalized Null Depth (dB)							
	Isotropic		Homogeneous		Tx-1×8B		Tx-1×8A	
θ_N	MDBF	LCMV	MDBF	LCMV	MDBF	LCMV	MDBF	LCMV
$-30°$	-20.6	-65.0	-21.0	-65.4	-18.7	-23.3	-18.0	-18.4
$-25°$	-25.2	-64.0	-25.1	-64.0	-38.4	-25.6	-25.1	-20.8
$-20°$	-13.9	-71.4	-14.6	-72.1	-17.1	-29.3	-18.5	-29.6
$-15°$	-13.8	-71.2	-15.8	-73.2	-17.2	-28.1	-25.8	-22.4
$-10°$	-31.2	-66.0	-33.6	-68.4	-22.2	-27.0	-10.2	-19.3
20°	-25.7	-60.2	-27.2	-61.7	-21.7	-34.7	-11.6	-27.8
25°	-14.5	-66.1	-16.3	-68.0	-16.3	-37.7	-27.7	-27.9
30°	-13.2	-70.0	-15.3	-72.0	-14.1	-32.0	-20.3	-27.5
Average	-19.8	-66.7	-21.1	-68.1	-20.7	-29.7	-19.6	-24.2

Table 3.1: Achieved Null Depths with Fixed $\theta_i = 5°$

For the Tx-1×8A sub-array, which presents higher radiation pattern variation, the average null depths achieved with LCMV are 5.5 dB lower than the Tx-1×8B case and 42 dB lower than in the isotropic scenario. This case shows less than -5 dB improvement in null depth through LCMV over MDBF. Notably, in 2 out of the 8 cases, LCMV performed worse than the MDBF benchmark.

These results show that increased variation in the radiation patterns among individual array elements correlates with more degraded performance by the LCMV beamformer. It aligns with our concern that it is harder to predict the statistical properties of incoming signals and derive a well-conditioned covariance matrix, as in (3.3), under large variations in antenna ERPs.

In the second phase, we modulated the primary beam angle (θ_i) across the $-30°$ to $30°$ range, with a static θ_N at $5°$. The results are represented in Table 3.2.

In isotropic and homogeneous pattern cases, LCMV improves nulling depth by -59.4 dB over the MDBF case. The Tx-1×8B case showed a 45 dB drop in LCMV performance compared to the uniform elements scenario, with an improvement of -15.7 dB over MDBF. The Tx-1×8A sub-array exhibited an even further performance degradation, with LCMV performing worse than MDBF by 0.9 dB on average and 59 dB lower than the isotropic scenario, reinforcing the correlation between element pattern variation and LCMV performance.

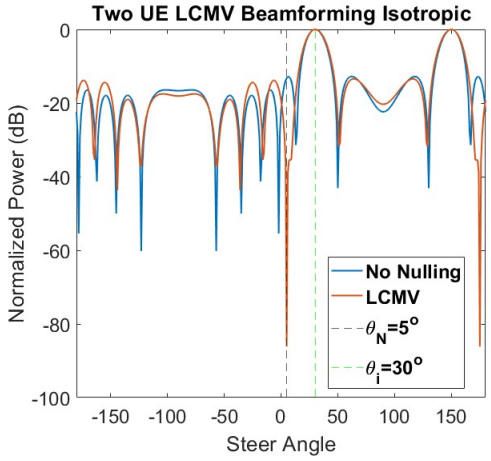

(a) Beam pattern using Isotropic ERP

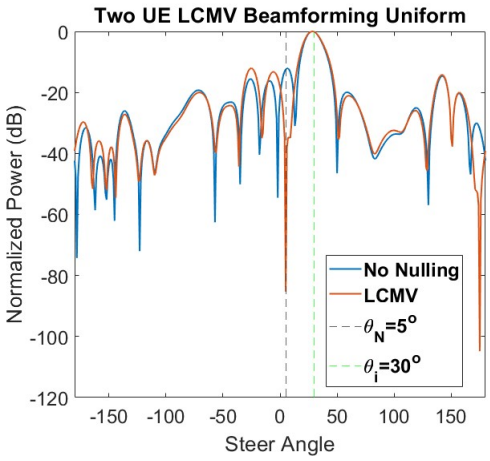

(b) Beam pattern using Uniform ERP

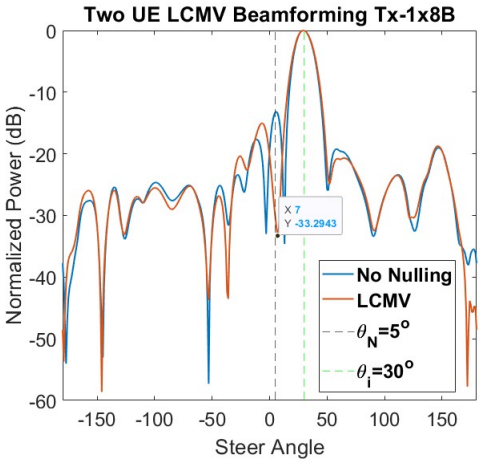

(c) Beam pattern using Tx-1x8B ERP

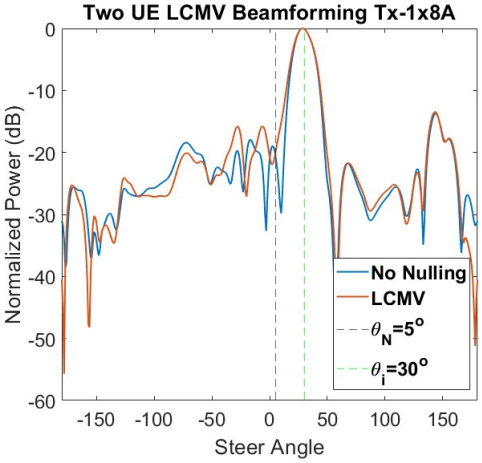

(d) Beam pattern using Tx-1x8A ERP

Figure 3.4: Tx 1x8 Beam Pattern comparison of LCMV Nulling in subarray with different ERP scenarios

A snapshot of the LCMV's performance across the four scenarios, assuming θ_i at 30° and θ_N fixed at 5°, is provided in Fig. 3.4. The figures clearly show that the deeper nulls are achieved in Isotropic and Homogeneous cases, however, in the rest of the two cases, the performance significantly decreases due to variation in ERP.

In conclusion, the simulation results show that in practical scenarios where the assumption of uniform ERP is no longer valid, LCMV may not accurately estimate the

	Normalized Null Depth (dB)							
	Isotropic		Homogeneous		Tx-1×8B		Tx-1×8A	
θ_i	MDBF	LCMV	MDBF	LCMV	MDBF	LCMV	MDBF	LCMV
$-30°$	-20.6	-81.3	-21.8	-82.6	-20.3	-34.7	-20.7	-20.2
$-25°$	-25.2	-77.7	-26.7	-79.2	-22.3	-34.5	-27.9	-29.8
$-20°$	-13.9	-81.4	-14.7	-82.3	-13.1	-32.9	-20.6	-24.6
$-15°$	-13.8	-83.4	-13.5	-82.9	-13.7	-34.0	-27.4	-19.2
$-10°$	-31.2	-72.5	-30.5	-71.9	-26.1	-38.1	-12.2	-17.5
20°	-25.7	-71.9	-25.4	-71.6	-22.9	-33.9	-13.0	-16.5
25°	-14.5	-79.1	-14.1	-78.7	-15.1	-32.8	-28.8	-16.2
30°	-13.2	-86.1	-12.4	-85.3	-13.1	-31.0	-20.4	-20.1
Average	-19.8	-79.2	-19.9	-79.3	-18.3	-34.0	-21.4	-20.5

Table 3.2: Achieved Null Depths with Fixed $\theta_N = 5°$

inverse covariance matrix and can converge to suboptimal beamforming coefficient resulting in a significantly poor performance.

3.2.3 LCMV performance based on user proximity

In this simulation, our objective is to determine the minimum angular separation between the desired user (θ_i) and the interference user (θ_N) that can be achieved by the LCMV algorithm without significantly distorting the overall beam pattern. This analysis helps to assess LCMV's effectiveness in suppressing interference located in close proximity to the intended user. For simplicity, we focused on a two-user scenario, utilizing the Tx-1 × 8B sub-array for the simulation.

The main steering angle was set to $\theta_i = 5°$, while the nulling angle was varied from $\theta_N = -30°$ to $\theta_N = 30°$ in increments of 5° (except for $\theta_N = 5°$). This was done to determine the closest possible proximity between the main beam and nulling directions before it influences the overall beam shape, such as the sidelobe levels and beam peak direction.

The simulation results in Table 3.3 indicate that as long as the separation $|\theta_i - \theta_N|$ remains greater than 15° (or 0.5 × First Null Beamwidth (FNBW)), the beam remains unaffected without any tilting or distortion. Additionally, sidelobe levels are kept below -12 dB, and the beam main lobe is accurately directed in the desired direction.

$\lvert\theta_N - \theta_i\rvert$	Directivity (dBi)	Normalized Null Depth (dB)	Normalized Sidelobe Level (dB)	Beam Peak Deviation from θ_i (degrees)
$-35°$	14.8	-23.3	-14.1	0
$-30°$	14.8	-25.6	-13.3	0
$-25°$	14.6	-29.3	-13.0	0
$-20°$	14.6	-28.1	-13.9	-1
$-15°$	14.8	-27.0	-13.3	0
$-10°$	14.1	-30.2	-7.8	3
$-5°$	9.9	-38.6	-4.0	7
$5°$	9.9	-30.6	-3.4	-6
$10°$	14.0	-29.6	-6.9	-3
$15°$	14.8	-34.7	-12.5	-1
$20°$	14.6	-37.7	-16.7	0
$25°$	14.6	-32.0	-15.5	0

Table 3.3: Directivity and Null Depth for Two-User Case $\theta_i = 5°$

On the other hand, if $|\theta_i - \theta_N| < 15°$, distortions in the beam shape emerge. The main beam tilts in the direction opposite to the null direction by up to 7°, resulting in a loss of power in the main user direction. Sidelobe levels also rise to approximately -7 dB or higher.

Fig. 3.5 provides an azimuth cut at 0° elevation angle for beams created using LCMV weights on the Tx-1×8B sub-array. The plots show the no-nulling (MDBF) scenario and 4 different nulling angle cases from the table. The plots confirm the increase in sidelobe levels and deviation of beam peak once the distance between the users is less than 15°.

To avoid beam distortion or tilting, it is essential to properly consider the nulling angle and its distance from the main beam, especially when applying LCMV weights to the sub-array. This can be achieved by taking into account the FNBW, which is influenced by the number of antenna elements in the array as shown in Fig. 2.2. A general criterion is established showing the correlation of separation distance to the average FNBW:

$$|\theta_i - \theta_N| > 0.5 \times \text{FNBW} \tag{3.5}$$

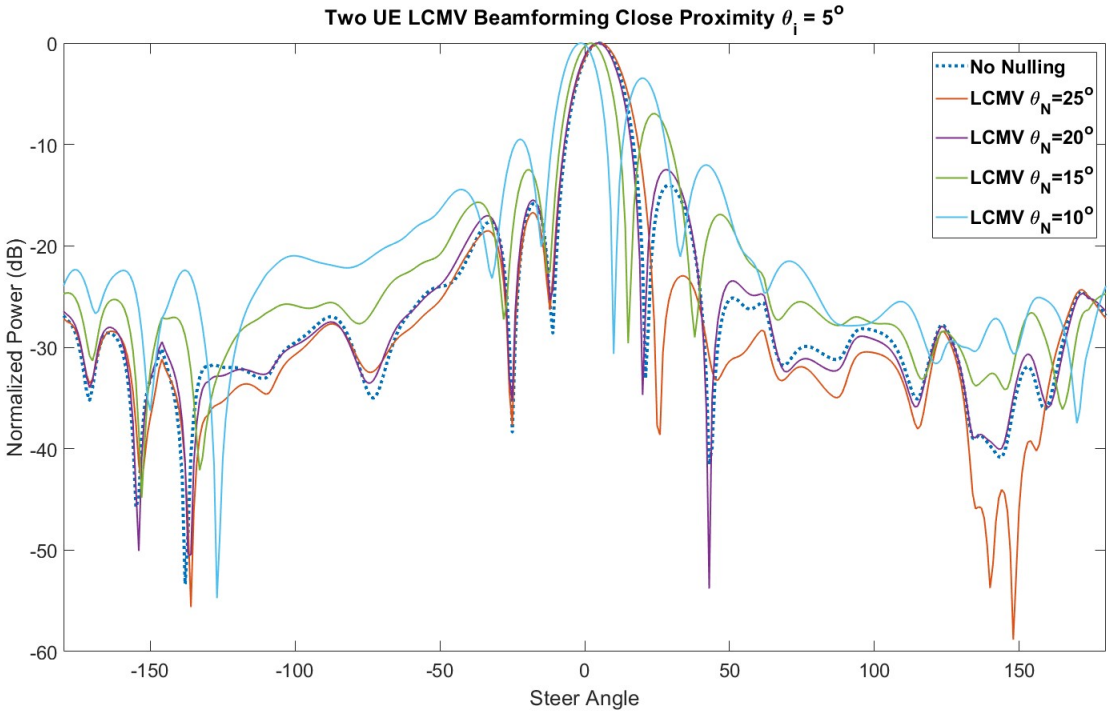

Figure 3.5: Beam patterns for Tx-1×8B, LCMV with $\theta_i = 5^o$ and varied θ_N

3.2.4 Exhaustive search for LCMV 2-User Case

This simulation was conducted to assess the LCMV beamforming algorithm's ability to achieve sufficient nulling depths (better than -20 dB) across various (θ_i, θ_N) pairings. The Tx-1 × 8B sub-array was selected for this purpose, with beamforming coefficients generated using the MATLAB LCMV toolbox.

An iterative approach was employed, where both θ_i and θ_N were varied from $-50°$ to $50°$ in $1°$ increments, leveraging the characteristics of the Tx-1 × 8B sub-array. The separation criterion defined in (3.5) was applied, which for this sub-array translated to a minimum angular separation of $15°$ between all (θ_i, θ_N) pairs.

The results of our extensive simulation are presented in Fig. 3.6, where pixel intensity reflects the depth of the nulls achieved. Darker pixels correspond to steering and nulling angle pairs that achieve normalized nulls deeper than the -20 dB threshold using the LCMV scheme, while white pixels denote (θ_i, θ_N) pairs where deep nulls could not be realized when

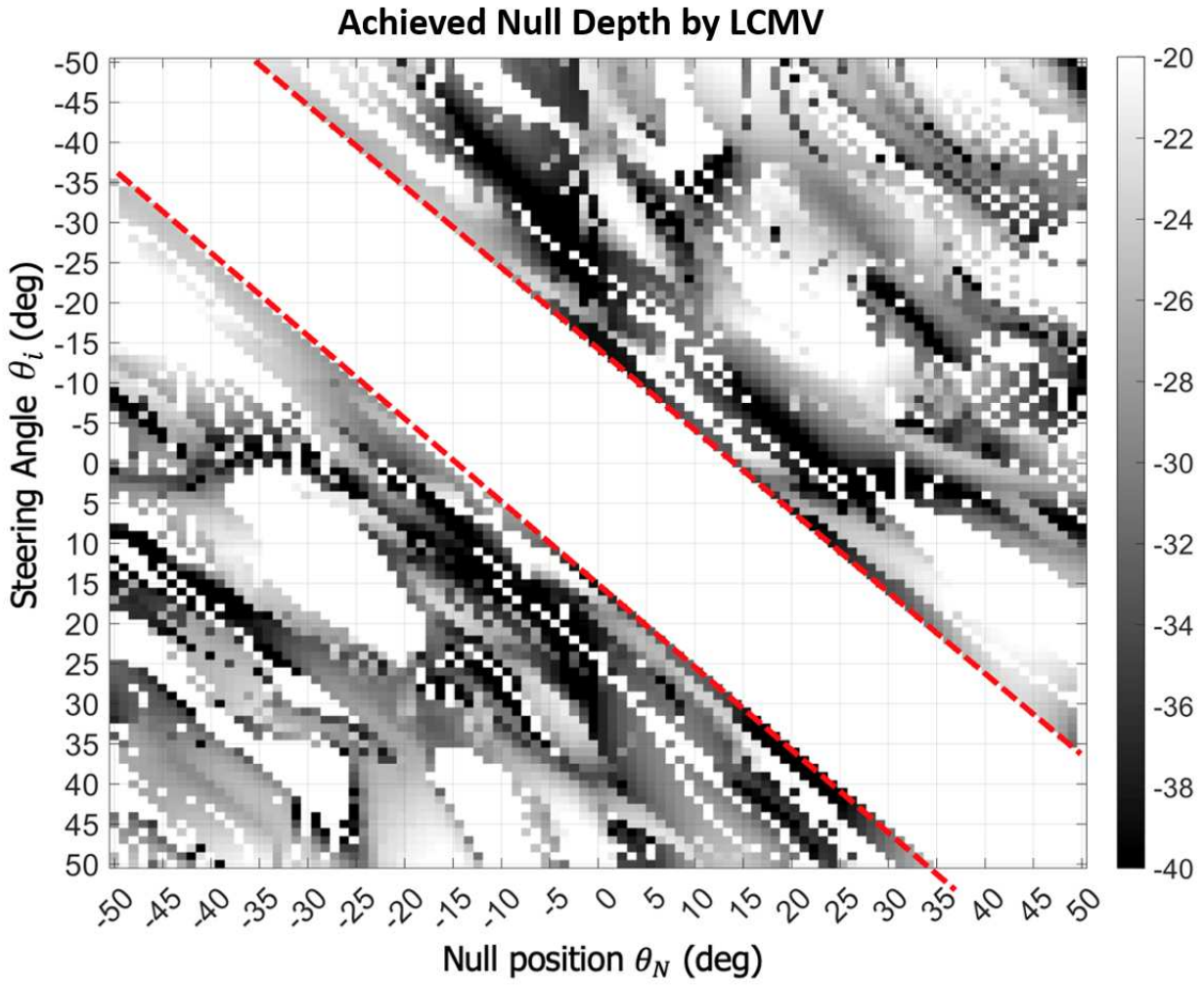

Figure 3.6: Nulling depths at different (θ_i,θ_N) locations (simulation results with Tx-1×8B)

applying LCMV weights to practical antenna elements.

The presence of several white patches indicates that LCMV failed to achieve deep nulls for certain angle pairs. In approximately 50% of the simulation cases, the normalized null depth was less than -20 dB, suggesting the sub-optimal performance of LCMV when applied to heterogeneous antenna elements in real-world scenarios. In areas where darker pixels appear, the null depths typically range between -20 dB and -35 dB.

Additionally, the simulations revealed that the LCMV algorithm often demonstrates inaccuracies in establishing precise nulls at the designated nulling angle θ_N, with deviations

of 1 to 3 degrees observed in the simulations.

3.2.5 LCMV performance under multiple interferences

This simulation was conducted to evaluate the impact of introducing additional nulls into the LCMV-generated beam pattern, aimed at testing the algorithm's capability to handle multiple interference sources. Given the degree of freedom constraint in a $1 \times M$ array, the algorithm can control up to $M - 1$ arbitrary nulls. However, for this simulation, up to three interference users were tested. The Tx-1 $\times$ 8B sub-array was chosen for the simulation and beamforming coefficients were generated using the MATLAB LCMV toolbox.

The main steering angle was set at $\theta_i = 10°$, and three arbitrarily selected nulls were introduced sequentially at angles $\theta_{N1} = -30°$, $\theta_{N2} = -10°$, and $\theta_{N3} = 30°$. The results can be visualized in Fig. 3.7.

In this simulation, each null was introduced sequentially to monitor how the addition of nulls impacted the overall beam profile and the depth of previous nulls. It was observed that adding a new null caused a noticeable shift in the beam peak away from its intended direction by up to 3°.

The achieved null depths ranged from -23 dB to -31 dB relative to the beam peak, averaging -26 dB, which is 8 dB lower than the average nulling achieved for the Tx-1×8B sub-array in single-user cases. This demonstrates that adding additional nulls or nullifying multiple interferences under practical antenna element conditions can impact LCMV performance in terms of precision and depth of nulls.

3.3 Concluding Remarks

This chapter has highlighted the impact of heterogeneous ERPs on the performance of the LCMV algorithm. Simulations have shown that LCMV performs suboptimally when the antenna elements of the array are non-uniform, resulting in shallower or less precise nulls, which can degrade overall system performance. Addressing this issue necessitates a solution that takes ERP variations into account when adjusting the LCMV coefficients.

In the next chapter, PNCB is introduced as a method to address the limitations of LCMV in the presence of heterogeneous ERPs. PNCB provides a robust mechanism for

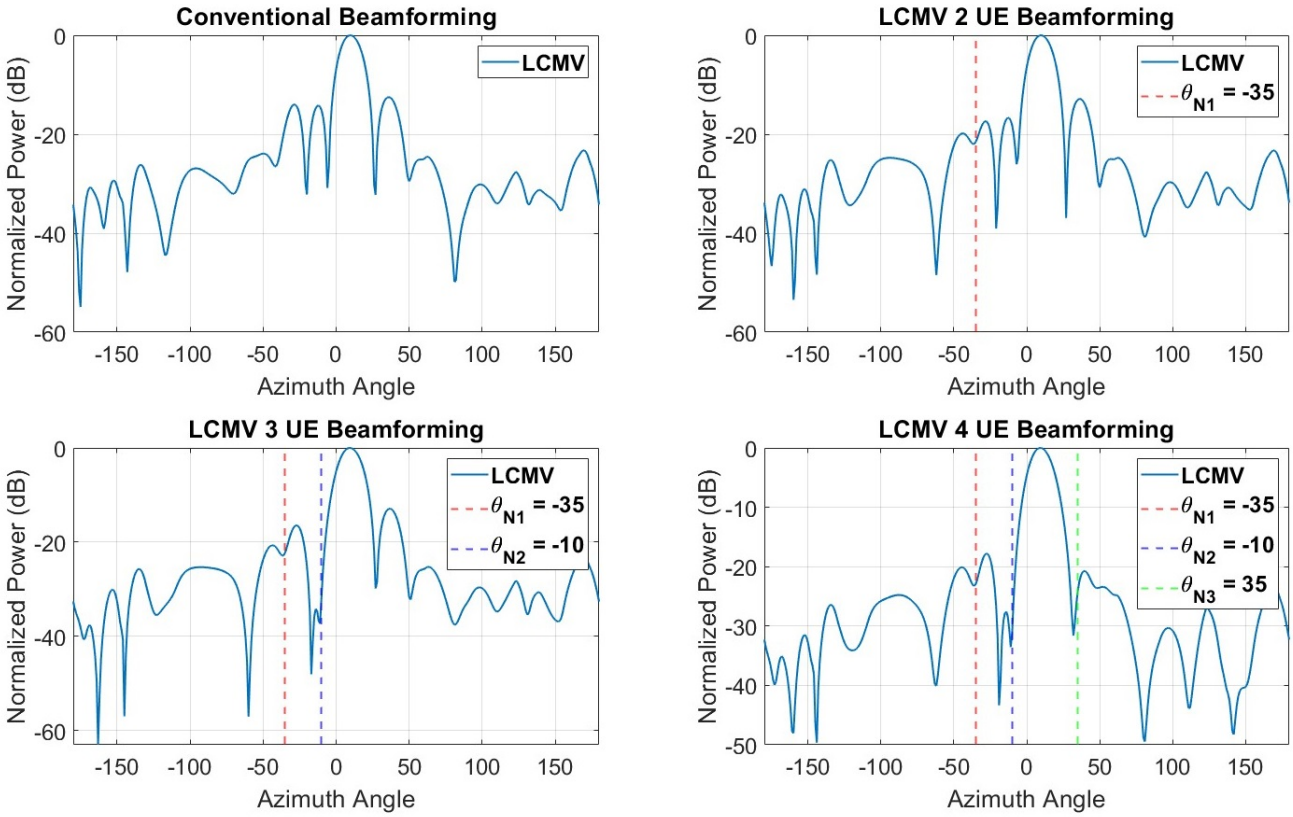

Figure 3.7: Beam radiation patterns with 0, 1, 2, 3 added nulls (simulation results using LCMV)

dynamically adjusting beamforming coefficients, ensuring optimal performance even with non-uniform antenna elements. The principles and implementation of PNCB will be discussed, demonstrating its effectiveness in overcoming the challenges faced by traditional LCMV beamforming in real-world scenarios.

Chapter 4

Perturbation Based Adaptive Beamforming [1]

As presented in the previous chapter, non-iterative ABF algorithms perform optimally with uniform ERP, as the estimated covariance matrix accurately captures the spatial characteristics of the incoming signal. However, in practical implementations, non-uniform radiation patterns of antenna elements introduce variations to complicate the precise estimation of the array response, leading to potential misalignment between the estimated and the actual response for both $\boldsymbol{a}_i(\theta_i, \phi_i)$ and $\boldsymbol{\mathcal{A}}_i(\boldsymbol{\theta}_N, \boldsymbol{\phi}_N)$. Within the framework of the LCMV algorithm, this misalignment often results in a poorly conditioned covariance matrix $\mathbf{R}_i(\boldsymbol{\theta}_N)$ calculated in (3.3), which does not accurately estimate the spatial properties of the incoming signal. As illustrated in the previous results, this limits the performance of LCMV by generating sub-optimal beamforming weights that produce shallow and imprecise nulls.

To address the limitations of LCMV beamforming in scenarios with heterogeneous antenna element patterns, a PNCB technique is proposed. This method enhances nulling performance by introducing fine perturbations to the LCMV-generated beamforming vectors. These perturbations adjust the beamforming weights to improve interference suppression by accommodating variations in ERPs. This technique traverses the search

[1] Parts of this chapter have been presented at the 2023 IEEE 98th Vehicular Technology Conference (VTC2023-Fall), Hong Kong, Hong Kong [1] and in the IEEE Open Journal of Vehicular Technology, vol. 5, pp. 1273-1293, 2024 [2]

space in search of optimum magnitude and phase values to update the beamforming vectors. The updated beamforming vectors are effective in NCB by adapting to ERP variation making this technique more practical in real-life scenarios where the antenna array has heterogeneous ERPs. However, as the number of antenna elements M increases, the complexity of deriving an optimal beamformer grows exponentially. For example, determining the optimal combination of α-level quantized magnitudes and β-level quantized phases for an M-element array through exhaustive search would require $\alpha^M \beta^M$ iterations, leading to a significant increase in computational complexity.

To reduce computational complexity, PSO is integrated into the PNCB framework as an efficient alternative to exhaustive search methods. The metaheuristic nature of PSO allows for more efficient exploration of larger solution spaces with reduced computational overhead. Its stochastic and parallel multi-agent search aspects make PSO particularly well-suited for tackling complex, non-convex optimization problems. PSO excels in navigating high-dimensional search spaces where traditional optimization techniques may struggle, consistently delivering robust solutions even in challenging scenarios, such as large-scale beamforming with multiple interference sources.

This chapter introduces the proposed PNCB scheme, explains the working principles of PSO within our model, and presents comparative simulation and measurement results to investigate the effectiveness of the method.

4.1 Proposed Particle Swarm Optimization for Nulling Control Improvement

In the proposed model, PSO is employed to search for the optimal beamforming solution while taking into consideration the individual ERPs of the antenna elements in the array. PSO is a nature-inspired algorithm designed to solve optimization problems by mimicking the social behaviour of swarms, such as flocks of birds or schools of fish. It operates by initializing a population of particles, each representing a potential solution, which in our case is a potential beamforming vector.

The algorithm operates by moving particles through the search space, confined within defined boundaries, with their positions being adjusted based on both their individual

experiences and the experiences of other particles in the swarm. Typically, the initial positions of these particles are randomly selected. However, to enhance the search process, we propose a PNCB strategy that integrates PSO with the LCMV beamformer for the initial generation of search vectors. By using an LCMV-derived vector $\mathbf{w}_{lcmv}(\theta_i, \boldsymbol{\theta}_N)$ as the starting point, PSO can converge toward more optimal solutions, mitigating the risk of premature convergence to local minima. This combined approach leverages the LCMV's strengths for rapid initial weight generation and the flexibility of PSO to refine the beamforming vectors further.

Since beamforming vectors consist of M complex weights, containing both magnitude and phase information, most approaches decompose these into real-value component vectors before applying optimization [32]. In our work, we decompose the beamforming vectors into a $2M$ real-value vector, which facilitates perturbations and allows separate search boundaries for phase and magnitude. Consequently, during the PSO search, each beamforming search vector is represented as:

$$\boldsymbol{\Omega}_p^n = [\text{mag}(\mathbf{w}_p^n), \text{ang}(\mathbf{w}_p^n)], \tag{4.1}$$

where $\boldsymbol{\Omega}_p^n \in \mathbb{R}^{2M}$ represents the search vector for the p^{th} particle at the n^{th} iteration, $\text{mag}(\mathbf{w}_p^n) \in \mathbb{R}^M$ denotes the magnitudes of the beamforming weights $\mathbf{w}_p^n \in \mathbb{C}^M$, and $\text{ang}(\mathbf{w}_p^n) \in \mathbb{R}^M$ corresponds to the phases of $\mathbf{w}_p^n$.

The initial search vector, derived from the LCMV beamformer, is expressed as:

$$\boldsymbol{\Omega}_p^1(\theta_i, \boldsymbol{\theta}_N) = \boldsymbol{\Omega}_{lcmv}(\theta_i, \boldsymbol{\theta}_N) = [\text{mag}(\mathbf{w}_{lcmv}(\theta_i, \boldsymbol{\theta}_N)), \text{ang}(\mathbf{w}_{lcmv}(\theta_i, \boldsymbol{\theta}_N))]. \tag{4.2}$$

For the proposed model, the scenario illustrated in Fig. 3.1 is considered, where an M-element i^{th} sub-array is operating in an environment with K active users. As shown in Fig. 4.1(a), our proposed algorithm initializes by taking the measured ERPs of the M elements, the target user's location θ_i, and the positions of potential interference sources $\boldsymbol{\theta}_N$, as inputs to the LCMV beamformer. For simplicity, the elevation angles of all users are fixed at $\phi = 90°$ for both simulations and measurements. The inputs are processed by the LCMV function to instantaneously generate the initial steering vector $\mathbf{w}_{lcmv}$, which serves as the initialization point for the subsequent PSO optimization process.

In the PSO optimization phase, shown in Fig. 4.1(b) N_p particles explore the solution

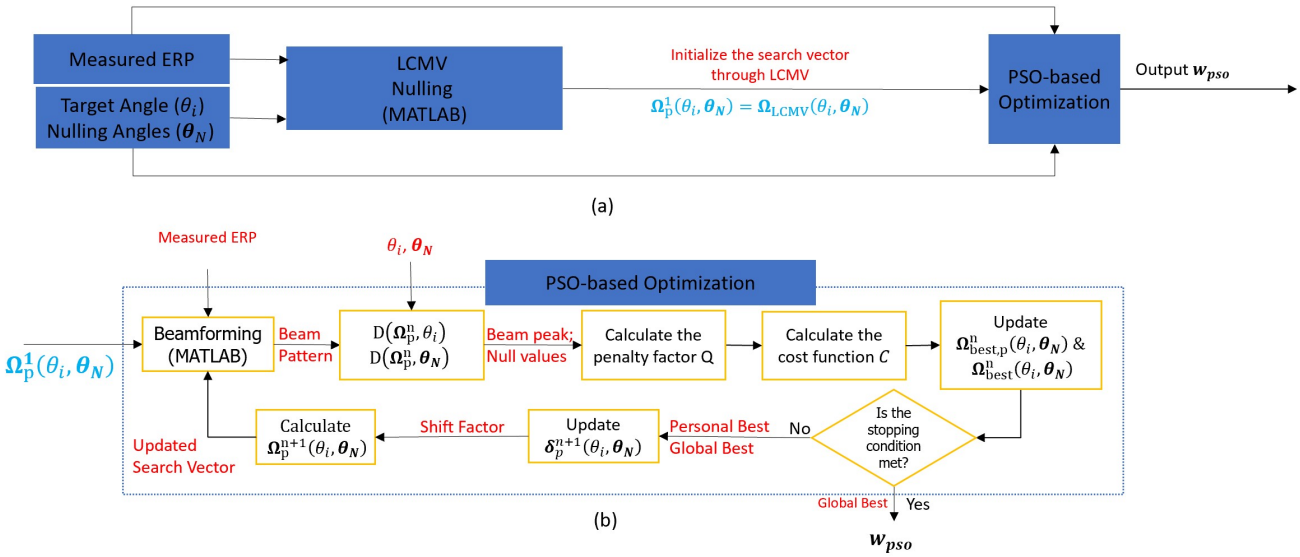

Figure 4.1: a) Flow diagram illustrating the integration of PSO with LCMV in the proposed PNCB; b) Iterative process of the PSO-based optimization block

space in parallel, updated iteratively over a maximum of N_n iterations. The computational complexity of PSO is governed by three primary parameters: the number of particles (N_p), the number of iterations (N_n), and the number of antenna elements (M). In each iteration, every particle evaluates the objective function, which has a complexity of $O(t(2M))$, where $t(2M)$ represents the time complexity of evaluating the cost function for the $2M$-dimensional input. Additionally, each particle updates its velocity and position, requiring basic arithmetic operations with a $O(2M)$ complexity. Therefore, the per-iteration complexity for all particles is $O(N_n[t(2M) + 2M)]$. Over N_n iterations, the total complexity becomes $O(N_p N_n[t(2M) + 2M)]$. If the objective function is simply polynomial as in our case, $t(2M)$ is typically $O(2M)$, leading to an overall complexity of $O(2MN_pN_n)$. However, for more complex functions (e.g., involving matrix operations), $t(2M)$ dominates the complexity.

The scalability of PSO makes it a viable approach for optimizing large-scale antenna arrays, where the problem dimensionality is given by $2M$. For large values of M, the increased dimensionality introduces a greater challenge in finding optimal solutions within a reasonable time frame. However, this challenge can be addressed through several improvements. Adaptive PSO variants, such as dynamic inertia weight adjustment and

constriction factor techniques, help improve convergence speed without compromising solution quality. Furthermore, parallel implementations of PSO can leverage modern computing architectures to efficiently distribute the computational workload, significantly reducing optimization time. Additionally, PSO's convergence behaviour can be controlled by adjusting the number of particles (N_p) and the number of iterations (N_n), allowing it to scale dynamically with problem size. Increasing these parameters can improve the precision of the solution but incurs a higher computational cost. Reducing them accelerates the process at the potential cost of solution accuracy.

Furthermore, leveraging the inherent symmetry of antenna arrays, as discussed in [2], can significantly reduce the dimensionality of the PSO optimization problem for large-scale arrays. By exploiting this symmetry, the number of weights that need to be optimized is reduced, leading to a lower computational cost without compromising performance. This reduction in dimensionality enhances the efficiency of PSO, making it more scalable for large-scale antenna array applications. Overall, PSO remains a powerful and adaptable optimization technique, and by integrating advanced PSO strategies and computational optimizations, it is possible to achieve high-performance solutions even as antenna array sizes continue to grow.

The primary objective of this optimization is to suppress interference in the directions specified by $\boldsymbol{\theta}_N$ while maintaining high directivity toward the target angle θ_i. To prevent the algorithm from converging on suboptimal beamforming vectors that degrade the SINR, a heavy penalty factor Q is introduced. This penalty ensures that particles are directed toward improving solutions during each iteration. The penalty factor evaluates the performance of the current search vector $\boldsymbol{\Omega}_p^n$ relative to the initial vector $\boldsymbol{\Omega}_{lcmv}$ and assigns a high value when the current search vector underperforms. Specifically, deviations in directivity beyond an allowable tolerance ϵ at the target angle θ_i, or insufficient null depth compared to the LCMV solution at the interference angles $\boldsymbol{\theta}_N$, trigger penalties. These penalty-incurring cases can be defined as:

$$\begin{aligned} &\text{Case 1:D}(\boldsymbol{\Omega}_p^n, \boldsymbol{\theta}_N) > \text{D}(\boldsymbol{\Omega}_{lcmv}(\theta_i, \boldsymbol{\theta}_N), \boldsymbol{\theta}_N), \\ &\text{Case 2:D}(\boldsymbol{\Omega}_p^n, \theta_i) \leq \text{D}(\boldsymbol{\Omega}_{lcmv}(\theta_i, \boldsymbol{\theta}_N), \theta_i) - \epsilon, \end{aligned} \tag{4.3}$$

where the function $\text{D}(\boldsymbol{\Omega}_p^n, \boldsymbol{\theta})$ represents the normalized directivity values evaluated at the

angle $\boldsymbol{\theta}$ for the search vector $\boldsymbol{\Omega}_p^n$ corresponding to the p^{th} particle at the n^{th} iteration. The output of D(.) is dimensionally equivalent to the variable $\boldsymbol{\theta}$.

As shown in Fig. 4.1(b), during each n^{th} iteration, all N_p search vectors $(\Omega_p^n(\theta_i, \boldsymbol{\theta}_N), \forall p = 1, \cdots, N_p)$ are used to compute their corresponding radiation directivity toward both the intended user and the interference users using the directivity function of MATLAB's Phased Array Toolbox. These results are then used to evaluate each particle's penalty factor Q based on defined cases in (4.3) as follows:

$$Q = \begin{cases} 0, & \text{if neither of the two case is true,} \\ Q_1, & \text{if one of the two cases is true,} \\ Q_2, & \text{if both the cases are true,} \end{cases} \tag{4.4}$$

where $0 < Q_1 < Q_2$ to signify a higher penalty where both cases are true.

Once the penalties are calculated, particles evaluate their current position using the following cost function, which determines how optimal or effective the solution is:

$$C(\boldsymbol{\Omega}_p^n) = \boldsymbol{\gamma}\mathrm{D}(\boldsymbol{\Omega}_p^n, \boldsymbol{\theta}_N) - \chi\mathrm{D}(\boldsymbol{\Omega}_p^n, \theta_i) + Q, \tag{4.5}$$

vector $\boldsymbol{\gamma} \in \mathbb{R}^{1\times(K-1)}$ and the scalar $\chi \in \mathbb{R}$ are arbitrary positive constants, with $\boldsymbol{\gamma} > 0$ and $\chi > 0$. The $\mathrm{D}(\boldsymbol{\Omega}_{lcmv}, \theta_i) \in \mathbb{R}$ denotes the directivity at the target angle θ_i, while $\mathrm{D}(\boldsymbol{\Omega}_{lcmv}, \boldsymbol{\theta}_N) \in \mathbb{R}^{K-1}$ gives the directivity at the interference nulling angles when the LCMV beamformer is applied. Therefore, in the cost function, any increase in target directivity or decrease in radiation power in the interference directions reduces the overall cost function value.

As the particles move through the solution space, each one keeps track of two important points: its personal best position, $\boldsymbol{\Omega}_{\text{best},p}^n$ for the p^{th} particle, which represents the best solution the particle has found so far, and the global best position, $\boldsymbol{\Omega}_{\text{best}}^n$, which represents the best solution found by any particle in the entire swarm. These two points guide the movement of the particles as they explore the search space, helping them to converge toward the optimal solution and can be written as:

$$\boldsymbol{\Omega}_{\text{best},p}^{n} = \underset{\boldsymbol{\Omega}_{p}^{(n^*)},\forall n^*=0,1,\cdots,N_n}{\arg\min} \; C\left(\boldsymbol{\Omega}_{p}^{(n^*)}\right),$$
$$\boldsymbol{\Omega}_{\text{best}}^{n} = \underset{\boldsymbol{\Omega}_{\text{best},p}^{n},\forall p=1,\cdots,N_p}{\arg\min} \; C\left(\boldsymbol{\Omega}_{\text{best},p}^{n}\right).$$

Once the cost value is computed, the stopping criterion is evaluated. Typically, the stopping criterion can be defined by a maximum of N_n iterations, a maximum number of stall iterations N_s (iterations without significant improvement in the cost function), a predefined threshold for the cost function, or a combination of these. When the stopping criterion is satisfied, the optimization process halts, and the current global best vector $\boldsymbol{\Omega}_{\text{best}}^{n}$ is output as the final solution. If the stopping criterion is not met, the optimization continues with the objective of minimizing the cost function, which can be formulated as:

$$\begin{aligned} \min_{\hat{\boldsymbol{\Omega}}} \quad & C(\hat{\boldsymbol{\Omega}}), \\ \text{s.t.} \quad & \text{Constraint 1: } \forall u \in \text{mag}(\hat{\mathbf{w}}), 0 \leq u \leq 1, \\ & \text{Constraint 2: } \text{ang}(\hat{\mathbf{w}}) \geq \text{ang}(\mathbf{w}_{lcmv}(\theta_i, \boldsymbol{\theta}_N)) - \Delta v, \\ & \text{and } \text{ang}(\hat{\mathbf{w}}) \leq \text{ang}(\mathbf{w}_{lcmv}(\theta_i, \boldsymbol{\theta}_N)) + \Delta v, \end{aligned} \tag{4.6}$$

where Constraint 1 sets the search boundary for the magnitude of each element in the beamforming vector, restricting it to the range $[0, 1]$. Constraint 2 defines the limits for phase perturbations, with Δv representing the maximum allowable phase variation from the initial LCMV beamformer phase $\text{ang}(\mathbf{w}_{lcmv}(\theta_i, \boldsymbol{\theta}_N))$. The value of Δv is chosen based on the largest permissible phase shift that still ensures an acceptable steering angle change in the main lobe.

The perturbation or velocity of each particle for the next $(n+1)$ iteration is governed by three main factors: its current velocity (denoted as $\boldsymbol{\delta}_p^n \in \mathbb{R}^{2M}$), the distance between its current position and its personal best $\boldsymbol{\Omega}_{\text{best},p}^{n}$, and the distance between its current position and the global best $\boldsymbol{\Omega}_{\text{best}}^{n}$. The current velocity component helps the particle maintain its direction and speed of movement, while the distances to both the personal best and global best enable the particle to adjust its trajectory. This mechanism ensures that particles are directed toward their own best-known solutions and the best solution identified by the

swarm, achieving a balance between the exploration of new regions and the exploitation of known promising areas. The updated velocity for the p^{th} particle is given by:

$$\boldsymbol{\delta}_p^{n+1} = \mathbf{J}\boldsymbol{\delta}_p^n + \mathbf{K}(\boldsymbol{\Omega}_{\text{best},p}^n - \boldsymbol{\Omega}_p^n) + \mathbf{L}(\boldsymbol{\Omega}_{\text{best}}^n - \boldsymbol{\Omega}_p^n), \tag{4.7}$$

where $\mathbf{K}$ and $\mathbf{L}$ are positive, random diagonal matrices that control the self-adjustment and social adjustment, respectively. These matrices regulate each particle's tendency to move toward its personal best ($\boldsymbol{\Omega}_{\text{best},p}^n$) and the global best ($\boldsymbol{\Omega}_{\text{best}}^n$) positions. The diagonal weight matrix $\mathbf{J}$ controls the inertia of the particle by scaling its current velocity.

Once the velocity vector is updated, it is critical to ensure that the new search vector remains within the defined boundaries. If the updated velocity causes the search vector to exceed these limits, it must be clipped to ensure that both the magnitudes and phases stay within the feasible region. To this end, we define a clipping function, clip(.), that strictly enforces these constraints by adjusting any component of the updated search vector that exceeds the allowable range back to the nearest boundary value. Hence, the update for the new beamforming search vector $\boldsymbol{\Omega}_p^{(n+1)}$ is expressed as:

$$\boldsymbol{\Omega}_p^{(n+1)} = \text{clip}(\boldsymbol{\delta}_p^{(n+1)} + \boldsymbol{\Omega}_p^n, \boldsymbol{\Omega}_L, \boldsymbol{\Omega}_U), \tag{4.8}$$

where $\boldsymbol{\Omega}_L, \boldsymbol{\Omega}_U \in \mathbb{R}^{2M}$ represent the lower and upper bounds of the search space, respectively, derived from the constraints stated in (4.6).

4.2 Simulation results for proposed PNCB method

In this section, we present the results of our simulations to assess the performance of our proposed method. It is important to note that null levels and nulling values reported in this section are expressed as normalized radiation power values in the target nulling directions, relative to the power level of the main lobe in the desired user directions. The power towards the desired user direction is taken as the reference point, corresponding to 0 dB. Moreover, the elevation angle for all azimuth cut plots shown are the same and fixed at the angle normal

to the subarray.

4.2.1 PNCB performance in two-user scenario

As discussed in the previous chapters, the ERP of array antenna elements plays a critical role in determining the performance of NCB algorithms. With increased variation in ERP, we observed that the LCMV algorithm's performance degrades, resulting in suboptimal beamforming precision and reduced efficacy. To further investigate how ERP variations impact the PNCB process, we conducted simulations on a Tx-1×8 sub-array under four distinct ERP scenarios:

i) **Isotropic**: All elements exhibit isotropic radiation patterns, providing an idealized scenario.

ii) **Homogeneous**: All elements have identical radiation patterns, with the central element (B4) representing the characteristics of the entire array.

iii) **Tx-1×8B**: Refers to the central 1×8 sub-array, where the radiation pattern variation among the elements is minimal.

iv) **Tx-1×8A**: Refers to the 1×8 sub-array located at the edge of the array, where there is significant variation in the radiation patterns of individual elements.

To evaluate the nulling performance of the proposed PNCB method in comparison to both the MDBF and LCMV beamforming techniques, beam pattern plots were generated for visual analysis. In these experiments, the primary beam was steered towards a target angle of $\theta_i = 30°$, while the nulling angle was set at $\theta_N = 5°$.

This comparative analysis offers critical insights into how different ERP assumptions affect beamforming accuracy, with a specific focus on nulling depth and the consistency of the beam shapes across various scenarios. By analyzing the performance of each method under the same conditions, the relative strengths and weaknesses in handling interference and shaping the radiation pattern can be better understood.

The cases of isotropic and homogeneous ERPs are shown in Figs. 4.2(a) and (b). In these scenarios, both assumptions enable the LCMV algorithm to compute optimal steering coefficients effectively, yielding deep radiation nulls exceeding -80 dB, accurately aligned with the target nulling angles. The beam patterns generated by the proposed PNCB method closely follow those produced by the LCMV beamformer, indicating comparable performance. The PNCB approach could not further optimize the weights, as

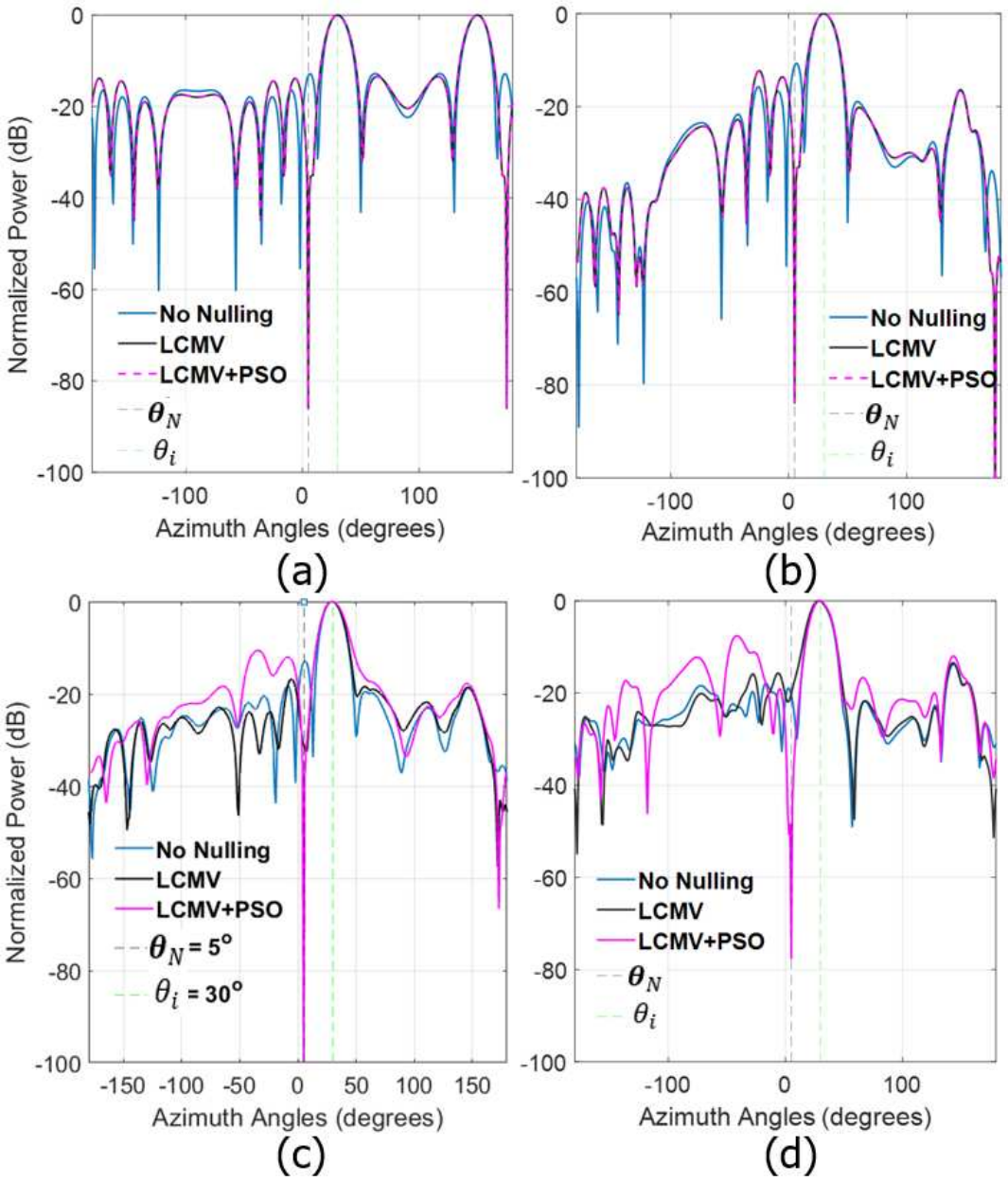

Figure 4.2: Beam pattern comparison for a 1x8 sub-array, with $\theta_i = 30°$ and $\theta_N = 5°$ under different ERP assumptions: (a) isotropic element pattern; (b) homogeneous element pattern; (c) Tx-1x8B; (d) Tx-1x8A.

the null depth and accuracy across both methods remained consistent, demonstrating the robustness of PNCB in environments with uniform element patterns.

When applied to measured heterogeneous element patterns, however, the performance of the LCMV algorithm degrades significantly, as discussed in Section 3.2.2. Fig. 4.2(c) reveals that for the central Tx-1×8B sub-array, LCMV achieves a null depth of approximately -31 dB. However, for the edge sub-array Tx-1×8A, shown in Fig. 4.2(d), the null depth deteriorates to -22 dB, with a deviation of around 3° from the intended nulling angle.

In contrast, the proposed PNCB method shows substantial improvement in both null depth and angular accuracy. For the Tx-1×8B sub-array, the PNCB achieves a null depth of -101.6 dB at the nulling angle $\theta_N = 5°$, representing a 70.6 dB improvement over the LCMV-based result. Additionally, the null is precisely positioned at the target angle of 5°, as opposed to LCMV, which produced the null at 7°. Regarding beam characteristics, PNCB produces a 3 dB beamwidth of 17° and a normalized sidelobe level of -10.6 dB, resulting in a slight beamwidth increase of 1° and a 2 dB rise in sidelobe level compared to LCMV.

For the Tx-1×8A sub-array, PNCB significantly enhances nulling performance, achieving a null depth of -77.6 dB at $\theta_N = 5°$, marking a 55 dB improvement over the LCMV-derived result. The PNCB also managed to correct the 3^o deviation in the null position and generated the null precisely at the desired θ_N.

These findings reconfirm the challenges faced by LCMV in maintaining deep nulls with precise angular control in environments where significant variations exist in the ERPs. As the discrepancies in ERP increase, the effectiveness of the LCMV algorithm in achieving accurate nulling deteriorates. Conversely, the PNCB method proves to be far more robust and effective in handling non-uniform ERPs, producing deeper and more accurately positioned nulls even in complex array configurations.

Performance of PSO for different θ_i, θ_N combinations

To assess the effectiveness of the perturbation-based method, we conducted eight test simulations using the Tx-1×8B sub-array. The steering angle (θ_i) was varied between $-30°$ and 30°, while the nulling angle (θ_N) was fixed at 5°. The simulation settings, including the array configuration and ERP values, were consistent with those used in previous LCMV simulations. These configurations ensure that the perturbation-based approach is evaluated under the same conditions as the LCMV method, allowing for a fair performance

		Beam Directivity (dB)			Normalized Null Depth (dB)			Nulling Improvement
θ_i	θ_N	MDBF	LCMV	LCMV+PSO	MDBF	LCMV	LCMV+PSO	$Null_{LCMV}$ - $Null_{LCMV+PSO}$
-30^o	5^o	13.7	13.6	13.1	-20.3	-34.7	-57.1	22.6
-25^o	5^o	13.9	14.1	13	-22.3	-34.5	-48.1	13.5
-20^o	5^o	14.1	13.9	13.5	-13.1	-32.9	-62.2	29.3
-15^o	5^o	14.2	13.9	13.6	-13.7	-34	-184.7	150.7
-10^o	5^o	14.5	14.5	14.2	-26.1	-38.1	-160.2	122
20^o	5^o	14.6	14.6	13.5	-22.9	-33.9	-96	62
25^o	5^o	14.6	14.5	13.6	-15.1	-32.8	-76.2	43.3
30^o	5^o	14.5	14.4	13.5	-13.1	-31	-101.6	70.6
Average		14.3	14.2	13.5	-18.3	-34	-98.3	64.3

Table 4.1: Beamforming directivity and null depth at different locations (simulation results)

comparison. For the PSO configuration, the PSO weights were initialized with $\mathbf{w}_{LCMV}$, with a particle count of $N_p = 200$ and the maximum number of stall iterations set to 5. The maximum directivity trade-off was allowed to $\epsilon = 1dB$ and no early stopping criterion was applied.

To ensure the nulling process did not significantly distort the main lobe, we enforced a minimum separation of at least 15° (equivalent to half the FNBW) between the peak of the main lobe and the target nulling position. This separation helps preserve the integrity of the main lobe while achieving deep nulls at the desired interference angles.

The detailed simulation results for beam directivity and null depth are summarized in Table 4.1, offering a comparative view of the PSO-based beamforming method and traditional LCMV.

Using the PSO-based approach, all eight beams successfully achieved null depths exceeding -48.1 dB in the desired interference direction. On average, the PSO-based beamforming method produced nulls that were 64.3 dB deeper compared to those obtained with the LCMV algorithm alone, with individual improvement of more than 13.5 dB in all cases. In comparison to the MDBF method, the average power delivered to the undesired user at 5° was reduced by more than 70 dB.

However, the introduction of perturbations led to a slight reduction in average directivity. Specifically, there was a 0.8 dB decrease in directivity compared to MDBF and a 0.7 dB decrease compared to the LCMV outcomes. This demonstrates a trade-off between achieving deeper nulls and maintaining beam directivity. While the perturbation-based NCB method offers a substantial average improvement of 22.9 dB in null depth, it comes at the cost of a

modest 0.7 dB reduction in directivity when compared to the LCMV strategy. This trade-off highlights the balance between interference suppression and maintaining the integrity of the main lobe in beamforming applications.

4.2.2 Impact of starting search vector on the performance of PNCB

The coefficients generated by the LCMV beamformer offer a highly accurate approximation of the optimal beamforming solution, making them an excellent starting point for further optimization. By applying slight perturbations to the LCMV-derived coefficients, the optimization process can more efficiently converge toward the global optimum. This approach reduces the likelihood of the PSO algorithm becoming trapped in local minima, which is a common challenge in high-dimensional, non-convex optimization problems.

A second key advantage of this method is that PSO when initialized with LCMV-based coefficients, has a higher probability of reaching the global optimum faster compared to other methods. This is due to the fact that LCMV already provides a near-optimal solution, requiring fewer adjustments during the optimization process. Therefore fewer iterations are typically needed for PSO to converge to the optimal point, which results in reduced computation time and lower resource consumption. This efficiency is particularly valuable in real-time applications or scenarios involving complex beamforming tasks, where both time and computational power are critical factors.

To validate this concept, we conducted PSO simulations across 14 distinct cases, comparing results between initializing with MDBF generated search vector $\mathbf{\Omega}_{MDBF}(\theta_i, \theta_N)$ and LCMV-based search vector $\mathbf{\Omega}_{LCMV}(\theta_i, \theta_N)$. These 14 cases were randomly selected from a pool where PSO successfully achieved null depths beyond -100 dB, ensuring that the scenarios presented sufficient complexity to challenge the optimization process and increase the likelihood of encountering local optima.

For these simulations, we employed a swarm size of 800 particles (N_p) to enhance convergence, set the maximum number of stall iterations to 8 and the ϵ value was set to 1 dB. Additionally, we implemented a stopping criterion to halt the optimization process once a normalized null depth threshold of -100 dB was reached. This prevented unnecessary computations and ensured that the optimization focused only on achieving the

		Normalized Null Depth (dB)		Optimization Time (sec)	
		$\mathbf{\Omega}_p^1(\theta_i, \theta_N)$			
θ_i	θ_N	$\mathbf{\Omega}_{LCMV}(\theta_i, \theta_N)$	$\mathbf{\Omega}_{MDBF}(\theta_i, \theta_N)$	$\mathbf{\Omega}_{LCMV}(\theta_i, \theta_N)$	$\mathbf{\Omega}_{MDBF}(\theta_i, \theta_N)$
-20^o	5^o	-100.1	-105.0	6510	7672
-20^o	15^o	-100.5	-56.1	8500	2669
-15^o	35^o	-106.7	-59.8	5993	2169
-10^o	-25^o	-104.0	-68.0	5715	4799
-5^o	10^o	-112.9	-89.8	10144	7594
0^o	35^o	-101.2	-102.2	7970	6757
0^o	-20^o	-101.3	-65.0	7290	3868
10^o	-5^o	-104.0	-105.9	5527	7184
15^o	35^o	-105.9	-62.2	8379	2171
20^o	-35^o	-106.9	-59.2	6396	2832
20^o	-10^o	-100.8	-100.1	4848	7820
20^o	-35^o	-106.9	-59.2	6396	2839
20^o	-20^o	-103.6	-73.5	5083	4320
25^o	-30^o	-101.1	-102.7	7074	6277
Average		-104.0	-79.2	6845	4927

Table 4.2: Achieved null depth and convergence time comparison with different initialization weights

desired performance.

The results, as shown in Table 4.2, clearly demonstrate the effectiveness of using LCMV-based initialization in guiding the PSO algorithm towards global optima more efficiently than initializing with MDBF coefficients. In simulations initialized with the MDBF search vector $\mathbf{\Omega}_{MDBF}(\theta_i, \theta_N)$, 9 out of the 14 cases failed to achieve the global optimum, resulting in an average null depth that was 24.8 dB shallower. In contrast, when initialized with LCMV generated search vector $\mathbf{\Omega}_{LCMV}(\theta_i, \theta_N)$, all 14 cases either reached the global optimum. Furthermore, in the 5 instances where both methods successfully reached the global optimum, the LCMV-based initialization led to a 10.5% reduction in average optimization time, highlighting a faster and more efficient convergence process.

These findings underscore the strategic advantage of using LCMV-derived coefficients as the initial starting point for PSO optimization. This approach not only accelerates the convergence process but also significantly improves the likelihood of reaching the optimal

solution, making it a more desirable approach.

4.2.3 PNCB performance in a multiple-user interference scenario

To evaluate the performance of the proposed PNCB technique in more complex MU environments, simulations were performed with one desired user and three interference users. The desired user was placed alternately at angles of $-35°$, $-10°$, $10°$, and $35°$, while the interference users were placed at the remaining three positions. The angular separation between the users was maintained at more than $20°$, exceeding half of the 1×8 array's FNBW ($0.5 \times \text{FNBW} = 15°$). This ensured that the nulling process did not distort the main lobe of the beam pattern.

For the simulation, the Tx-1×8B ERPs were used while the configuration was kept consistent with the previous section with $N_p = 200$, max stall iterations set to 5, $\epsilon = 1$ and no early stopping criteria. Fig. 4.3 presents the simulation plots for the different steering and nulling angle combinations.

In the absence of nulling (MDBF), the average normalized radiation power level in the direction of the interference users was measured at -15.7 dB, with power levels fluctuating between -12.1 dB and -26.1 dB. The corresponding beam patterns exhibited an average directivity of 14.3 dB and an average 3dB-beamwidth of 15.4°.

With the LCMV beamforming approach, a modest improvement in interference mitigation was observed. The nulling depths ranged from -22.0 dB to -37.6 dB, with an average nulling depth of -27.6 dB, representing an improvement of 11.9 dB compared to the MDBF case. However, the achieved nulling angles deviated by an average of 2.5 degrees from the intended angles, with a maximum deviation of 8 degrees, which indicates some loss of precision in null placement.

In contrast, the proposed PNCB method exhibited substantial improvements in reducing radiation toward the interference directions. Across all four evaluated angle combinations, the nulling levels were consistently below -52.4 dB, with an average deviation of less than 0.5 degrees from the target nulling angles. The null depths ranged from -52.4 dB to -154.9 dB, providing a significant buffer for practical implementation challenges, such as phase shifter and attenuator quantization losses.

Compared to the MDBF and LCMV approaches, the PNCB method demonstrated significant enhancements in interference suppression. On average, the PNCB scheme

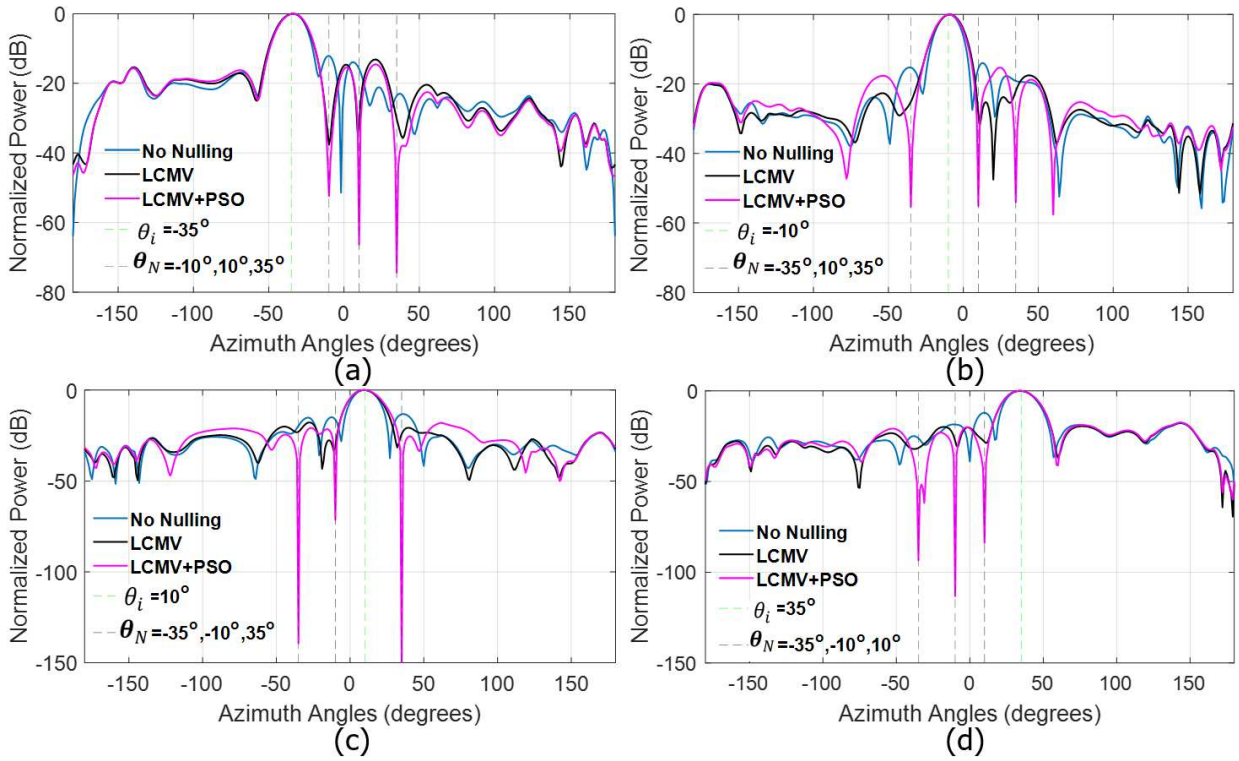

Figure 4.3: Beam radiation patterns for four-user cases (simulation results with Tx-1×8B

resulted in nulls that were 53.3 dB deeper than those achieved by MDBF and 41.4 dB deeper than those achieved by LCMV. The worst-case improvements in nulling depth were 40.3 dB and 30.4 dB, compared to the MDBF and LCMV cases, respectively.

In terms of beam characteristics, the PNCB method achieved an average directivity of 13.9 dB and a 3dB-beamwidth of 16.9°. While the PNCB approach resulted in a slight increase in beamwidth, ranging from 0.6 to 2.2 degrees compared to the MDBF, the impact on the main lobe's directivity was minimal. Across all test cases, the degradation in directivity was less than 0.6 dB, highlighting the PNCB method's ability to maintain robust main lobe characteristics while significantly improving nulling performance.

These results show the effectiveness of the PNCB method in delivering superior nulling performance with minimal impact on main lobe characteristics even in scenarios of multiple interferences. This makes it a robust solution for MUI suppression in beamforming applications.

4.2.4 Effect of Quantization on the PNCB performance

In simulation results, the PSO algorithm operates on a continuous search space for attenuator and phase shifter values, enabling thorough exploration and efficient convergence to the global optimum. However, in practical implementations, phase shifters and attenuators have finite resolution, resulting in a discrete search space. This discretization limits the precision of the solution, complicating the PSO algorithm's ability to converge to the global minimum.

To incorporate the discrete search space, quantization was applied by rounding the perturbed values to the nearest possible discrete value. However, quantization effects from the limited resolution of digital phase shifters and attenuators introduce errors, constraining the precision of steering coefficient adjustments and affecting overall beamforming performance. To evaluate this impact on PNCB's performance, different quantization scenarios were tested, providing insights into how resolution limitations influence the algorithm's ability to achieve optimal beamforming accuracy.

Simulations were conducted using the 1×8B sub-array, incorporating realistic quantization levels. The effect of Q_p-bit phase shifters and Q_t-bit attenuators on the achievable nulling depth was evaluated. A single nulling scenario, using 20 randomly selected (θ_i, θ_N) pairs where $|\theta_i - \theta_N| > 15^\circ$ to avoid main lobe interference, was used for meaningful comparison. Quantization levels for Q_p and Q_t were varied from 4 to 8 bits and infinity level was added for comparison. The average nulling depth for each combination is presented in Fig. 4.4, providing insights into how quantization affects beamforming precision.

The results reveal a strong correlation between reduced quantization levels and diminished nulling depth. As the resolution of the phase shifters (Q_p) and attenuators (Q_t) decreases, a marked degradation in nulling performance is observed. Specifically, reducing both Q_p and Q_t from infinite resolution to 4 bits results in an average nulling depth loss of 42.4 dB. The decline in performance is particularly steep in the lower quantization range, but it stabilizes as Q_p and Q_t increase. For example, with 6-bit phase shifters and 7-bit attenuators, the normalized average null depth drops from -70.7 dB (infinity resolution) to -41.7 dB, representing a 29 dB reduction.

Notably, phase shifters have a more pronounced impact on nulling precision. They are crucial for aligning the phases across antenna elements, enabling constructive and destructive interference for optimal beamforming. Reduced phase shifter resolution causes

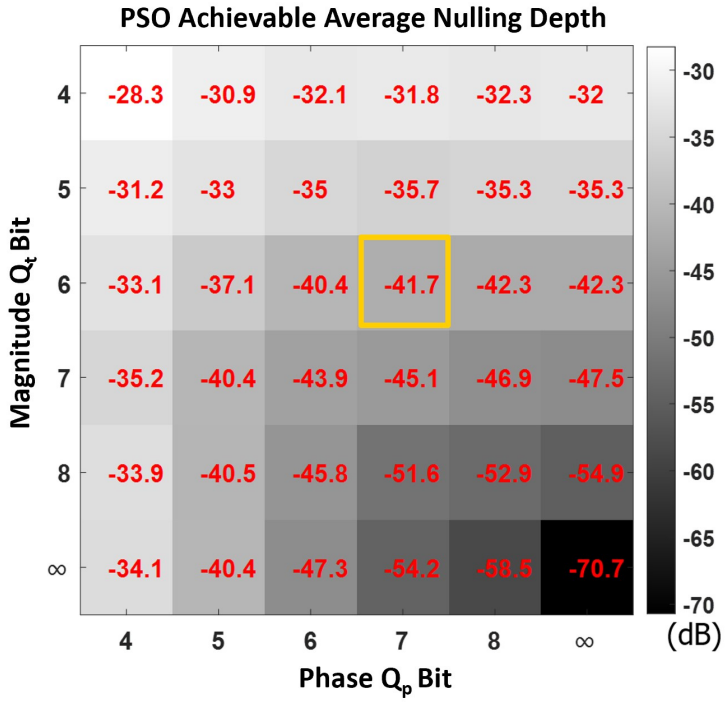

Figure 4.4: Average achievable nulling level (dB) versus the number of phase shifter and attenuator quantization bits (simulation results).

angular deviations in the beam pattern, leading to mismatches between the intended and actual nulling angles. Each bit reduction in Q_p results in a 4 to 7 dB decrease in null depth, especially in the range where $Q_p \geq 5$ and $Q_t \geq 8$.

In contrast, attenuator resolution has a stronger influence on the achievable nulling depth. Attenuators control the radiation power of each antenna element in specific directions, and precise attenuation enhances destructive interference, resulting in deeper nulls. With infinite Q_p resolution, reducing each bit of quantization in Q_t causes a significant drop of 3 to 7 dB for $Q_t \leq 8$.

These findings are crucial for beamforming system design, emphasizing the need for careful consideration of phase shifter and attenuator resolutions to maintain effective nulling performance. The trade-off between cost and performance is evident, as lower quantization levels lead to significant nulling degradation. When comparing these simulation results to practical measurements, the measured average null depth of -34.5 dB as compared to the

expected -41.7 dB, accounting for external factors and quantization effects. This confirms that higher quantization levels result in improved null depth performance in PSO-based beamforming.

4.3 Experimental Measurement

4.3.1 Experiment Setup

To evaluate the practical effectiveness of the PNCB method, experiments were conducted in an anechoic chamber, utilizing a Tx antenna board and two UE antennas as receivers. An 8×8 antenna array, representing the BS, was paired with two monopole antenna probes that simulated the UEs. The system implemented a partially connected hybrid beamforming scheme, with each RF chain connected to a subset of antenna elements grouped into sub-arrays. Each antenna sub-array is equipped with its own unique beam pattern, managed by a dedicated beamforming network. This setup benefits from reduced power cost and hardware complexity while maintaining the effectiveness of beamforming through each sub-array.

The antenna array was mounted on a motorized positioner, allowing precise rotation around the θ-angle to enable fine adjustments in the array's orientation relative to the UEs. This configuration facilitated a thorough assessment of the PNCB method's ability to suppress interference across various angular combinations (θ_i, θ_N), where θ_i and θ_N denote the angular positions of the desired user and the interfering user, respectively.The antenna configuration are shown in Figures 4.6, 4.7a, and 4.7b. The probe antennas that simulated the two UEs were separated by an angular distance of 22° ($|\theta_i - \theta_N| = 22°$), to ensure that both were equidistant from the center of the matrix. The Tx array and probe antennas were located within an anechoic chamber measuring 6.1 m × 2.4 m × 2.4 m (length × width × height), which was equipped with C-RAM SFC-48 RF absorbers to minimize reflections and external interference.

The experimental setup, shown in Fig. 4.5, utilizes the Tx-1×8B antenna sub-array at the BS integrated with a Beamforming Network Controller (BFNC) for signal transmission. The BFNC is programmed via a Raspberry Pi 4B (RPI-4B) to transfer control vectors to the designated phase shifters and attenuators.

The RPI-4B was selected as the processing unit due to its onboard memory, standalone

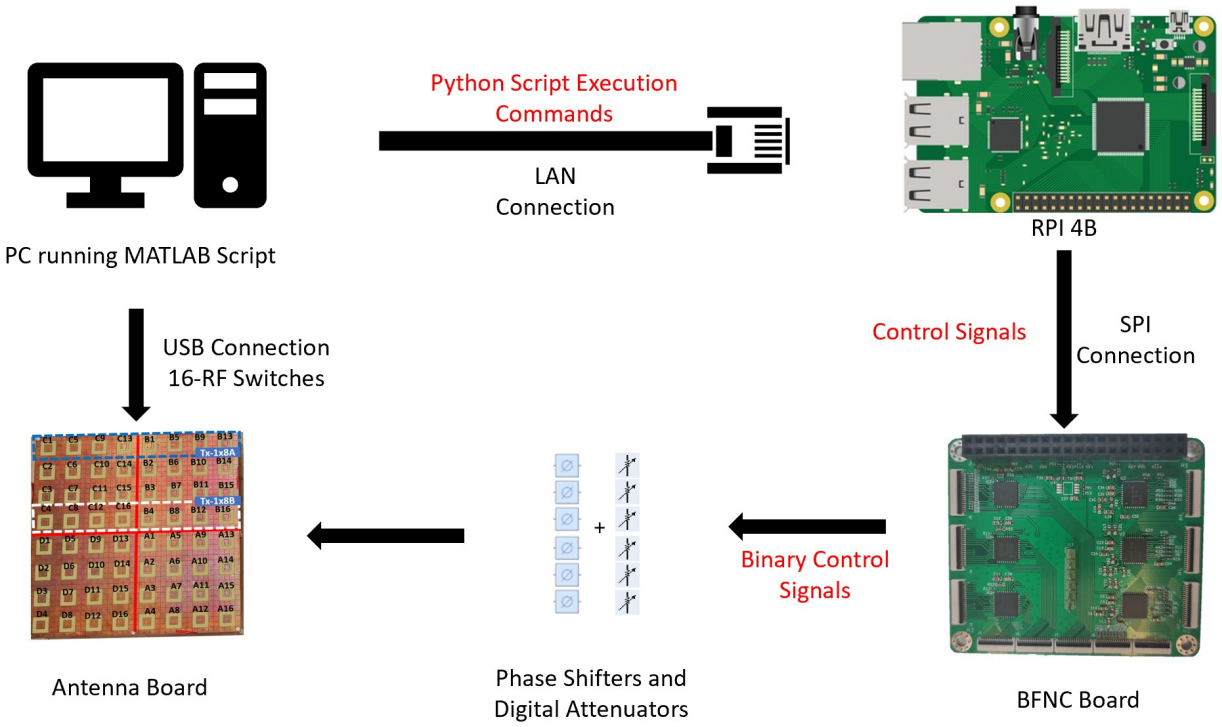

Figure 4.5: Measurement system connection using BFNC and RPi4B

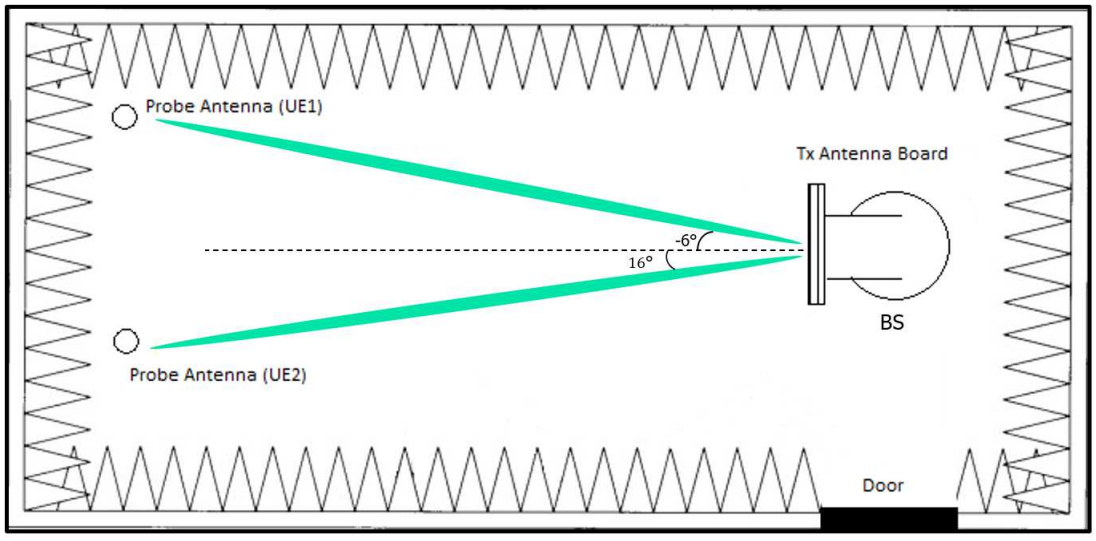

Figure 4.6: Design for Measurement Setup inside the Anechoic Chamber

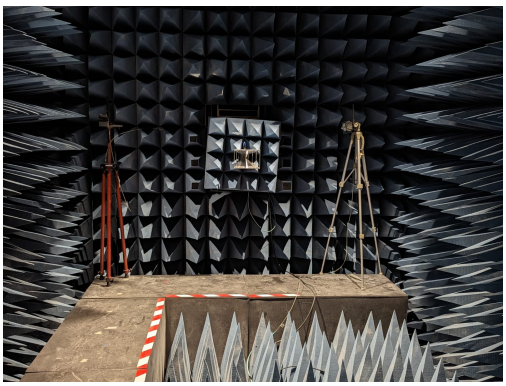

(a) Two antenna probes as viewed from the Base Station

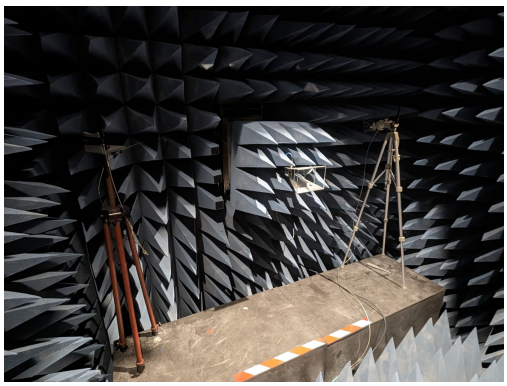

(b) Close-up side view of the two antenna probes

Figure 4.7: Positions of Two Rx Probe Antennas inside the Anechoic Chamber

processing capabilities, and ability to run Python on a Linux-based OS. It provides up to four independent SPI connections, which communicate with the BFNC board. The system interfaces with the RPI through the "MATLAB Support Package for Raspberry Pi Hardware" and an ethernet connection allowing data exchange and command execution. MATLAB on the PC connects to and runs Python scripts on the RPI-4B to perform tasks such as enabling Serial-to-Parallel Converter (SPC) and Digital-to-Analog Converter (DAC) chips (connected to SPI-0 and SPI-6) located on the BFNC. The RPI-4B further performs the tasks of configuring SPC registers, activating DAC registers and optionally programming DAC registers for analog phase shifter and attenuator voltage control by running the Python scripts. RPI-4B transfers the control signals through the SPI to set a 6-bit control vector for phase shifters and an 8-bit control vector for digital attenuators,

The BFNC, as shown in Fig. 4.8, includes three DACs for analog phase shifters and attenuator control, three SPCs for 6-bit digital phase shifters, and two XRA1404 chips (SPI-based 8-bit I/O expanders) for 7-bit digital attenuators. The BFNC is managed by a custom controller utilizing the Raspberry Pi's integrated SPI module. A single BFNC can control up to 16 phase shifters and attenuators, supporting configurations for subarrays of up to 16 antenna elements. The phase shifters provide full 360° phase control in 5.625° increments, while the attenuators allow up to 32 dB attenuation with 0.25 dB steps. All SPCs and DACs operate in a daisy-chain configuration, with the BFNC communicating over four SPI

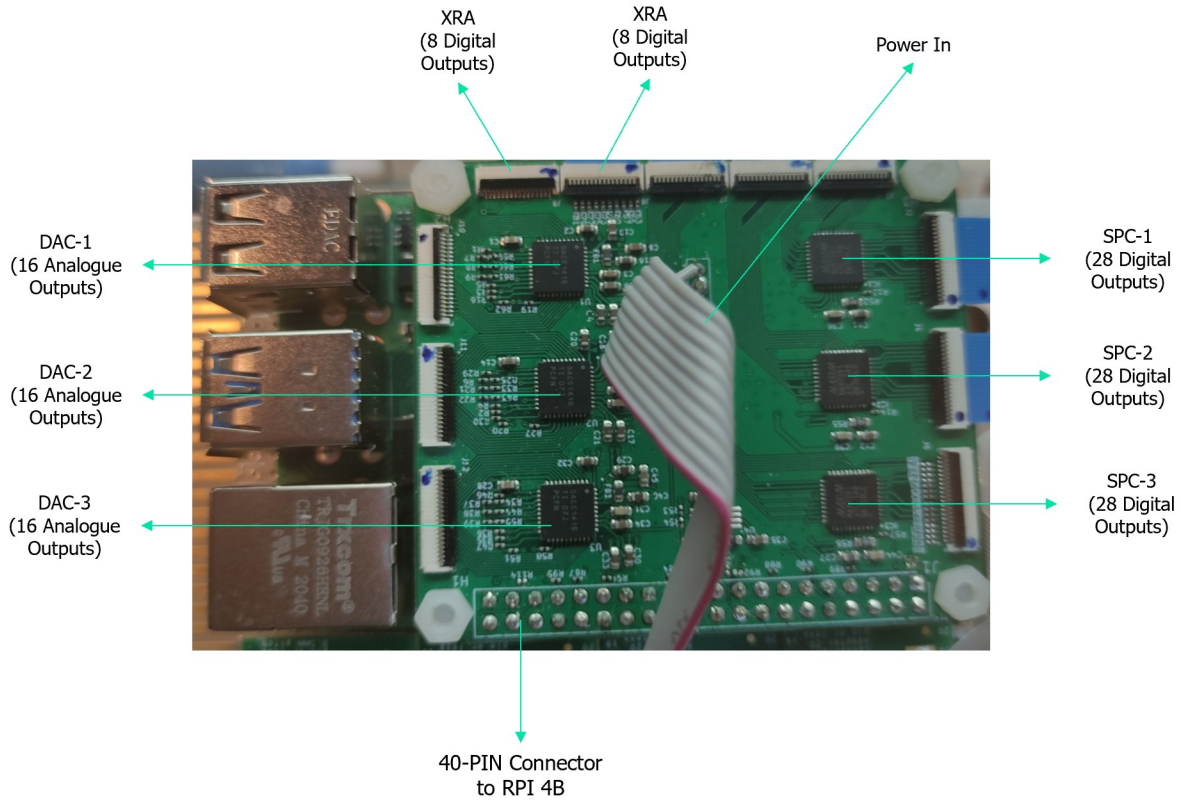

Figure 4.8: DAC, SPC and XRA chips located on the BFNC

connections. The components were interconnected using short coaxial cables and compact JSC connectors, strategically positioned behind the antenna array.

To compensate for system insertion loss, RF amplifiers were deployed prior to signal transmission. The experiments used a modulated NR-FR1-TM3.1 test signal, covering a 20 MHz bandwidth from 3.49 GHz to 3.51 GHz, with a transmission power of 10 dBm through the Tx sub-array.

The steering weights computed from the MDBF, LCMV, and PSO algorithms, using MATLAB on a PC, were applied to adjust the phase shifters and attenuators via RPI-4B and BFNC connections, allowing for dynamic control of the beam pattern within the anechoic chamber. The MDBF and LCMV weights were pre-calculated offline and served as benchmark comparisons for the PSO algorithm, with the LCMV weights also used as the initial search point for the PSO optimization process.

For the PSO algorithm, the beamforming coefficients were updated iteratively, incorporating real-time feedback from spectrum analyzers connected to the two UEs. This feedback was used by the PSO algorithm to compute the objective function within the optimization loop, allowing fine-tuning of the quantized beamforming coefficients to achieve optimal performance. The PSO was configured with 500 particles ($N_p = 500$), and the stall iteration limit was set to 5. No early stopping criteria were employed, and the directivity trade-off threshold was set to $\epsilon = 3$ dB.

4.3.2 Experiment Results

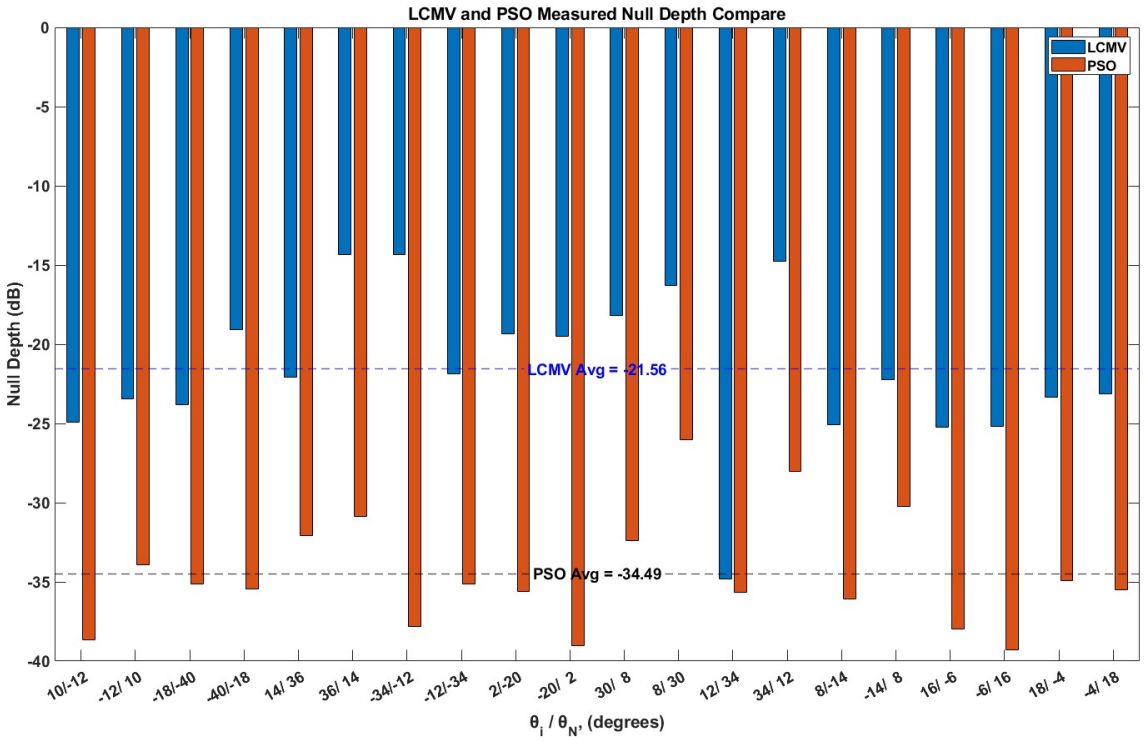

Figure 4.9: Measurement Results for LCMV and PSO Null Depth at different UE Angles

In the experiment, 10 angle combinations (totalling 20 measurements) that performed best in simulations were tested. As presented in Fig. 4.9 and tabulated in Table 4.3, the proposed NCB approach significantly improved the nulling depth in all 20 measurement scenarios.

The PSO algorithm demonstrates a clear advantage over the MDBF and LCMV methods, both in terms of null depth and power retention at the desired user (UE1). On average, PSO achieved a significantly deeper null depth of -34.5 dB, compared to -12.9 dB for MDBF and -21.6 dB for LCMV, translating to average improvements of 21.5 dB over MDBF and 12.9 dB over LCMV. The most substantial improvement in null depth using PSO over MDBF occurred in the scenario where $\theta_i = -34°$ and $\theta_N = -12°$, with a difference of 28.8 dB, while the largest improvement over LCMV was 23.4 dB in the same scenario. Even in the least improved case, for the angle pair ($\theta_i = 12°$, $\theta_N = 34°$), PSO still surpassed LCMV by 0.9 dB and MDBF by 23.4 dB. This consistent improvement across all scenarios highlights PSO's ability to deliver precise interference suppression under various conditions.

When analyzing the range of null levels achieved, PSO consistently outperformed the other methods across all measurements. The range of normalized null depths for MDBF varied from -7.7 dB to -19.3 dB, while LCMV achieved a range between -14.3 dB and -25.2 dB. In contrast, PSO exhibited significantly deeper nulls, with null depths ranging from -26 dB to -39.3 dB. This vast range, with a maximum null depth of -39.3 dB, emphasizes PSO's capability to achieve more precise and significant interference reduction. Additionally, the consistency of PSO's deeper nulls across all angle pairs underscores its robustness in mitigating interference effectively, regardless of the scenario.

PSO also maintained power at the desired user, with an average of -40.6 dB, slightly lower than MDBF (-37.1 dB) by 2.5 dB and LCMV (-38.6 dB) by 2 dB. This indicates that PSO not only performed better in suppressing interference but also preserves the desired signal strength under the given threshold of $\epsilon = 3dB$. Overall, PSO achieves a deeper range of nulls while maintaining the desired signal's integrity, making it a superior choice for beamforming applications that require interference suppression.

4.4 Concluding Remarks

This chapter presented the proposed PNCB method within the practical context of heterogeneous ERP. The PNCB approach incorporates measured element patterns and uses LCMV-generated steering coefficients as the starting point for PSO-based optimization. In simulations, PNCB significantly outperformed LCMV, achieving nulls that were 64 dB deeper in two-user cases and 41 dB deeper in four-user cases in interference directions.

		Power @ UE1 (dB)			Normalized Null Depth (dB)				
UE1 θ_i	UE2 θ_N	MDBF	LCMV	PSO	MDBF	LCMV	PSO	PSO – MDBF	PSO - LCMV
10	-12	-35.8	-37.7	-38.4	-17.9	-24.9	-38.7	-20.8	-13.7
-12	10	-37.6	-38.7	-40.4	-10	-23.5	-33.9	-23.9	-10.4
-18	-40	-35.6	-37.1	-39.8	-19.3	-23.8	-35.2	-15.9	-11.3
-40	-18	-40.6	-40.5	-42.3	-7.7	-19.1	-35.4	-27.7	-16.3
14	36	-38.2	-40	-41.7	-15.9	-22.1	-32.1	-16.1	-10
36	14	-37.5	-37.5	-40.3	-9.7	-14.3	-30.9	-21.2	-16.5
-34	-12	-39.4	-39.9	-42.4	-9	-14.4	-37.8	-28.8	-23.4
-12	-34	-35.7	-37	-39.2	-17.6	-21.9	-35.1	-17.6	-13.3
2	-20	-35.4	-41.6	-41.4	-16.8	-19.4	-35.6	-18.8	-16.2
-20	2	-37.7	-39.6	-41.5	-10.7	-19.5	-39	-28.3	-19.5
30	8	-36.3	-37.1	-39.8	-11.9	-18.2	-32.4	-20.5	-14.2
8	30	-38	-40.2	-42.8	-8.9	-16.3	-26	-17.1	-9.7
12	34	-38.3	-40	-42.9	-12.3	-34.8	-35.7	-23.4	-0.9
34	12	-37.1	-37.3	-40.3	-10.7	-14.8	-28	-17.3	-13.2
8	-14	-35.9	-37.3	-38.7	-17.1	-25.1	-36.1	-19	-11
-14	8	-37.7	-39	-41.1	-9.2	-22.2	-30.3	-21.1	-8
16	-6	-35.5	-36.8	-38.1	-16.1	-25.2	-38	-21.9	-12.7
-6	16	-37.4	-39	-40.3	-10.4	-25.2	-39.3	-28.8	-14.1
18	-4	-35.6	-36.4	-38.9	-15.7	-23.4	-34.9	-19.3	-11.6
-4	18	-37.5	-39.2	-42	-12	-23.2	-35.5	-23.4	-12.3
Average		-37.1	-38.6	-40.6	-12.9	-21.6	-34.5	-21.5	-12.9

Table 4.3: Power and Null Depth (Measured Results in Anechoic Chamber)

PNCB also achieved higher precision in null placement with an average deviation of less than 0.6 dB compared to a 3 to 8 dB deviation in the case of LCMV.

Experimental validation in an anechoic chamber reinforced these findings, with PNCB delivering 12.9 dB deeper nulls compared to LCMV in two-user scenarios, demonstrating its superior capability for interference mitigation. Although there was a minor tradeoff in directivity (0.6 dB in simulations and 2.5 dB in experiments), PNCB consistently provided higher SINR across all tested cases. This balance between minimal directivity loss and substantial interference suppression underscores PNCB's effectiveness in beamforming applications requiring precise interference control.

Chapter 5

Conclusions

5.1 Concluding Remarks

With the increasing demand for wireless resources and densely packed user environments, mitigating inter-user interference while maintaining signal strength for target users is crucial. This thesis develops an optimized null steering method for MU-mMIMO hybrid beamformers that outperforms existing techniques like LCMV under realistic ERP conditions.

The thesis begins by reviewing existing NCB methods, particularly LCMV, and investigates how heterogeneous ERPs impact its performance. Measured ERP data from an 8x8 dual-layer EBG array with a CP patch antenna array was used to represent real-life variations. Simulations demonstrated that LCMV's null depth declined by 37 to 59 dB as ERP variations increased, and it failed to achieve a 20 dB null depth in 50% of the scenarios, with inaccuracies up to 3 degrees in null positioning. In multi-user scenarios, LCMV struggled to maintain high SINR and accurate beamforming, with up to a 3-degree error in the main beam position when adding multiple nulls.

This thesis introduced a PNCB method to overcome these challenges, integrating LCMV with PSO to iteratively refine beamforming weights. The PNCB method dynamically adjusts LCMV-generated weights by adding perturbation and iteratively calculating the defined cost function through PSO. The PNCB outputs weights that provide optimal interference suppression while accounting for non-uniform ERPs and quantization limitations. Simulations showed that PNCB achieved nulls that were 64 dB deeper in two-user cases and 41 dB deeper in four-user cases compared to LCMV, with

higher precision in null placement. Experimental validation in an anechoic chamber further supported these findings, with PNCB delivering nulls 12.9 dB deeper than LCMV in two-user scenarios. Despite a minor tradeoff in directivity, 0.6 dB in simulations and 2.5 dB in experiments, PNCB consistently achieved higher SINR, demonstrating its effectiveness in interference mitigation.

In conclusion, PNCB provides a robust and practical solution for overcoming LCMV's limitations in environments with non-uniform ERPs and multiple interfering users. By refining beamforming weights through PSO, PNCB enhances null depth, precision, and overall system performance, making it an effective tool for advancing mMIMO systems in real-world, multi-user environments.

5.2 Potential Future Works

Although the proposed PNCB method effectively addresses the challenges of heterogeneous ERP in NCB methods, further improvements can be made to enhance its practical applicability. Below are some potential areas for future work:

- This thesis employs PSO to determine global optimum weights for achieving the deepest possible null at unintended users. However, the absence of an early stopping criterion may lead to prolonged convergence times. Future work could involve modifying the PSO setup to include early stopping criteria based on the maximum number of iterations (N_n) and/or minimum required null depth, ensuring that the PSO terminates once sufficient SINR is achieved.

- Currently, the PSO optimization process in this thesis uses two criteria, defined in (4.3), to impose penalties on the cost function. Future modifications could include additional criteria, such as sidelobe levels or 3dB beamwidth, to further constrain the generated beam shape. This could help to achieve a more robust radiation pattern in scenarios where sidelobe level and beamwidth can be important factors.

- The optimized weights generated by PNCB could serve as a training dataset for supervised learning models, such as a Deep Neural Network or Convolutional Neural Network. Leveraging these models would allow for the direct generation of optimized

weights based on the input parameters, eliminating the need for iterative optimization and reducing time and computational overhead.

Furthermore, PSO can also be integrated with other ABF algorithms to overcome their inherent limitations. For instance, the MVDR beamformer effectively minimizes interference while preserving the desired signal. However, its performance deteriorates in the presence of array imperfections, mutual coupling, and steering vector mismatches , making it less reliable in real-world applications. By incorporating PSO, the beamforming weight vectors can be dynamically optimized to account for these uncertainties. The optimization typically involves maximizing the SINR while penalizing deviations from the ideal steering vector, resulting in a more robust and interference-resistant beamformer.

Similarly, a combined implementation of LMS-PSO and RLS-PSO can improve performance in rapidly changing environments. The LMS and RLS algorithms update the beamforming weights in a stepwise manner based on incoming signal statistics. While effective in stable conditions, they suffer from slow convergence and instability in highly dynamic or noisy environments. PSO can address these issues by optimizing key parameters, such as the step size in LMS or the forgetting factor in RLS, allowing for faster adaptation without compromising stability. In this combined approach, the cost function typically minimizes the MSE between the desired output and the actual beamformer output while limiting parameter variations to prevent instability.

By leveraging the global search capability of PSO, these combined techniques can achieve faster convergence, improved robustness, and enhanced interference mitigation, making them suited for real-world ABF applications.

Bibliography

[1] Y. Gong, A. Yaseen, R. Morawski, and T. Le-Ngoc, "Perturbation-Based Adaptive Beamforming for MU-mMIMO," in *2023 IEEE 98th Vehicular Technology Conference (VTC2023-Fall)*, pp. 1–5, IEEE, 2023.

[2] Y. Gong, A. Yaseen, T. Zhang, R. Morawski, and T. Le-Ngoc, "Perturbation-Based Nulling Control Beamforming With Measured Element Radiation Patterns for MU-mMIMO," *IEEE Open Journal of Vehicular Technology*, vol. 5, pp. 1273–1293, 2024.

[3] R. Chataut and R. Akl, "Massive MIMO Systems for 5G and Beyond Networks—Overview, Recent Trends, Challenges, and Future Research Directions," *Sensors*, vol. 20, no. 10, p. 2753, 2020.

[4] F. Rusek, D. Persson, B. K. Lau, E. G. Larsson, T. L. Marzetta, O. Edfors, and F. Tufvesson, "Scaling Up MIMO: Opportunities and Challenges with Very Large Arrays," *IEEE Signal Processing Magazine*, vol. 30, no. 1, pp. 40–60, 2013.

[5] C. Doan, S. Emami, D. Sobel, A. Niknejad, and R. Brodersen, "Design considerations for 60 GHz CMOS radios," *IEEE Communications Magazine*, vol. 42, no. 12, pp. 132–140, 2004.

[6] I. Ahmed, H. Khammari, A. Shahid, A. Musa, K. S. Kim, E. De Poorter, and I. Moerman, "A Survey on Hybrid Beamforming Techniques in 5G: Architecture and System Model Perspectives," *IEEE Communications Surveys and Tutorials*, vol. 20, no. 4, pp. 3060–3097, 2018.

[7] I. Ahmed, H. Khammari, and A. Shahid, "Resource Allocation for Transmit Hybrid Beamforming in Decoupled Millimeter Wave Multiuser-MIMO Downlink," *IEEE Access*, vol. 5, pp. 170–182, 2016.

[8] W. L. Stutzman and G. A. Thiele, *Antenna Theory and Design*. John Wiley & Sons, 2012.

[9] C. A. Balanis, *Antenna Theory: Analysis and Design*. John Wiley & Sons, 2015.

[10] L. Zhang, W. Liu, and R. J. Langley, "Adaptive Beamforming with Real-Valued Coefficients Based on Uniform Linear Arrays," *IEEE Transactions on Antennas and Propagation*, vol. 59, pp. 1047–1053, Mar 2011.

[11] M. Khosravi, M. Fakharzadeh, and M. H. Bastani, "Large Array Null Steering Using Compressed Sensing," *IEEE Signal Processing Letters*, vol. 23, pp. 1032–1036, Aug 2016.

[12] J. A. Srar, K.-S. Chung, and A. Mansour, "Adaptive Array Beamforming Using a Combined LMS-LMS Algorithm," *IEEE Transactions on Antennas and Propagation*, vol. 58, pp. 3545–3557, Nov 2010.

[13] Y. Chen, T. Le-Ngoc, B. Champagne, and X. Changjiang, "Recursive Least Squares Constant Modulus Algorithm for Blind Adaptive Array," *IEEE Transactions on Signal Processing*, vol. 52, pp. 1452–1456, 2004.

[14] J. Capon, "High-Resolution Frequency-Wavenumber Spectrum Analysis," *Proceedings of the IEEE*, vol. 57, pp. 1408–1418, Aug 1969.

[15] L. Yang, M. R. McKay, and R. Couillet, "High-Dimensional MVDR Beamforming: Optimized Solutions Based on Spiked Random Matrix Models," *IEEE Transactions on Signal Processing*, vol. 66, pp. 1933–1947, Apr 2018.

[16] X. Wang, M. Amin, and X. Cao, "Analysis and Design of Optimum Sparse Array Configurations for Adaptive Beamforming," *IEEE Transactions on Signal Processing*, vol. 66, pp. 340–351, Jan 2018.

[17] M. Wax and Y. Anu, "Performance Analysis of the Minimum Variance Beamformer in the Presence of Steering Vector Errors," *IEEE Transactions on Signal Processing*, vol. 44, pp. 938–947, Apr 1996.

[18] D. Li, Q. Yin, P. Mu, and W. Guo, "Robust MVDR Beamforming Using the DOA Matrix Decomposition," in *2011 1st International Symposium on Access Spaces (ISAS)*, pp. 105–110, 2011.

[19] M. Robinson and I. Psaromiligkos, "Robust Minimum Variance Beamforming with Dual Response Constraints," in *2006 Fortieth Asilomar Conference on Signals, Systems and Computers*, pp. 2276–2280, 2006.

[20] L. Chang and C.-C. Yeh, "Performance of DMI and Eigenspace-Based Beamformers," *IEEE Transactions on Antennas and Propagation*, vol. 40, pp. 1336–1347, Nov 1992.

[21] M. W. Ganz, R. Moses, and S. Wilson, "Convergence of the SMI and the Diagonally Loaded SMI Algorithms with Weak Interference (Adaptive Array)," *IEEE Transactions on Antennas and Propagation*, vol. 38, pp. 394–399, Mar 1990.

[22] J. Li, P. Stoica, and Z. Wang, "On Robust Capon Beamforming and Diagonal Loading," *IEEE Transactions on Signal Processing*, vol. 51, no. 7, pp. 1702–1715, 2003.

[23] X. Mestre and M. Lagunas, "Finite Sample Size Effect on Minimum Variance Beamformers: Optimum Diagonal Loading Factor for Large Arrays," *IEEE Transactions on Signal Processing*, vol. 54, pp. 69–82, Jan 2006.

[24] I. Frost, O. L., "An Algorithm for Linearly Constrained Adaptive Array Processing," *Proceedings of the IEEE*, vol. 60, pp. 926–935, Aug 1972.

[25] B. R. Breed and J. Strauss, "A Short Proof of the Equivalence of LCMV and GSC Beamforming," *IEEE Signal Processing Letters*, vol. 9, pp. 168–169, Jun 2002.

[26] J. Xiong, H. Hong, H. Zhang, N. Wang, H. Chu, and X. Zhu, "Multi-Target Respiration Detection with Adaptive Digital Beamforming Technique Based on SIMO Radar," *IEEE Transactions on Microwave Theory and Techniques*, vol. 68, pp. 4814–4824, Nov 2020.

[27] S. D. Sonmasundaram, "Linearly Constrained Robust Capon Beamforming," *IEEE Transactions on Signal Processing*, vol. 60, pp. 5845–5856, Nov 2012.

[28] R. C. de Lamare, M. Haardt, and R. Sampaio-Neto, "Blind Adaptive Constrained Reduced-Rank Parameter Estimation Based on Constant Modulus Design for CDMA

Interference Suppression," *IEEE Transactions on Signal Processing*, vol. 52, pp. 2470–2482, 2008.

[29] Y. Cai and R. C. de Lamare, "Low-Complexity Variable Step-Size Mechanism for Code-Constrained Constant Modulus Stochastic Gradient Algorithms Applied to CDMA Interference Suppression," *IEEE Transactions on Signal Processing*, vol. 57, pp. 313–323, 2009.

[30] W. P. M. N. Keizer, "Fast Low-Sidelobe Synthesis for Large Planar Array Antennas Utilizing Successive Fast Fourier Transforms of the Array Factor," *IEEE Transactions on Antennas and Propagation*, vol. 55, no. 3, pp. 715–722, 2007.

[31] G. K. Mahanti, V. V. B. Bikkani, and S. K. Mandal, "Placement of Wide Nulls in the Radiation Pattern of a Linear Array Antenna Using Iterative Fast Fourier Transform," in *2012 IEEE International Conference on Signal Processing, Communication and Computing (ICSPCC 2012)*, pp. 552–555, 2012.

[32] K. Guney and M. Onay, "Amplitude-only pattern nulling of linear antenna arrays with the use of bees algorithm," *Progress in Electromagnetics Research-PIER*, vol. 70, 2007.

[33] M. M. Khodier and C. G. Christodoulou, "Linear Array Geometry Synthesis with Minimum Sidelobe Level and Null Control Using Particle Swarm Optimization," *IEEE Transactions on Antennas and Propagation*, vol. 53, pp. 2674–2679, Aug 2005.

[34] S. K. Goudos, V. Moysiadou, T. Samaras, K. Siakavara, and J. N. Sahalos, "Application of a Comprehensive Learning Particle Swarm Optimizer to Unequally Spaced Linear Array Synthesis with Sidelobe Level Suppression and Null Control," *IEEE Antennas and Wireless Propagation Letters*, vol. 9, pp. 125–129, 2010.

[35] A. Hamza and H. Attia, "Fast Beam Steering and Null Placement in an Adaptive Circular Antenna Array," *IEEE Antennas and Wireless Propagation Letters*, vol. 19, pp. 1561–1565, Sep 2020.

[36] M. R. Khan and V. Tuzlukov, "Null Steering Beamforming for Wireless Communication System Using Genetic Algorithm," in *Proceedings of the IEEE International Conference on Microwave Technology and Computational Electromagnetics*, pp. 289–292, 2011.

[37] D. W. Boeringer and D. H. Werner, "Particle Swarm Optimization Versus Genetic Algorithms for Phased Array Synthesis," *IEEE Transactions on Antennas and Propagation*, vol. 52, no. 3, pp. 771–779, 2004.

[38] J. Robinson, S. Sinton, and Y. Rahmat-Samii, "Particle Swarm, Genetic Algorithm, and Their Hybrids: Optimization of a Profiled Corrugated Horn Antenna," in *IEEE Antennas and Propagation Society International Symposium (IEEE Cat. No.02CH37313)*, vol. 1, pp. 314–317 vol.1, 2002.

[39] V. Zuniga, A. T. Erdogan, and T. Arslan, "Adaptive Radiation Pattern Optimization for Antenna Arrays by Phase Perturbations Using Particle Swarm Optimization," in *2010 NASA/ESA Conference on Adaptive Hardware and Systems*, pp. 209–214, 2010.

[40] S. Darzi, T. Sieh Kiong, M. Tariqul Islam, M. Ismail, S. Kibria, B. Salem, *et al.*, "Null Steering of Adaptive Beamforming Using Linear Constraint Minimum Variance Assisted by Particle Swarm Optimization, Dynamic Mutated Artificial Immune System, and Gravitational Search Algorithm," *The Scientific World Journal*, vol. 2014, 2014.

[41] T. Datta and I. S. Misra, "A Comparative Study of Optimization Techniques in Adaptive Antenna Array Processing: The Bacteria-Foraging Algorithm and Particle-Swarm Optimization," *IEEE Antennas and Propagation Magazine*, vol. 51, no. 6, pp. 69–81, 2009.

[42] D. H. Johnson and D. Dudgeon, *Array Signal Processing*. Englewood Cliffs, NJ: Prentice Hall, 1993.

[43] H. L. Van Trees, *Optimum Array Processing: Part IV of Detection, Estimation, and Modulation Theory*. John Wiley & Sons, 2002.

[44] B. Salem, S. K. Tiong, and S. P. Koh, "Beamforming Algorithms Technique by Using MVDR and LCMV," *World Applied Programming*, vol. 2, no. 5, pp. 315–324, 2012.

[45] M. Souden, J. Benesty, and S. Affes, "A Study of the LCMV and MVDR Noise Reduction Filters," *IEEE Transactions on Signal Processing*, vol. 58, pp. 4925–4935, Sep 2010.

[46] Y. Gong, R. Morawski, H. H. Lee, and T. Le-Ngoc, "A Miniaturized 8×8 Dual-Layer EBG Slotted Circularly Polarized Patch Antenna Array for mMIMO," in *2022 IEEE Global Communications Conference (GLOBECOM)*, pp. 6511–6516, Dec 2022.